Biosensors and Bioelectronics 308 (2026) 118757

Contents lists available at ScienceDirect

Biosensors and Bioelectronics

journal homepage: www.elsevier.com/locate/bios

Fast fourteen-frequency impedance spectroscopy of single erythrocytes and yeast cells in flow

Marta Righetto [a,1], Riccardo Reale [a,1], Federico Carneri [b], Alessandra Mistretta [c], Marta De Zotti [d], Daniela Roversi [b], Paolo Bisegna [a], Adele De Ninno [c], Federica Caselli [a,*]

[a] Department of Civil Engineering and Computer Science, University of Rome Tor Vergata, Rome, Italy
[b] Department of Chemical Science and Technologies, University of Rome Tor Vergata, Rome, Italy
[c] Institute for Photonics and Nanotechnology, Italian National Research Council, Rome, Italy
[d] Department of Chemical Sciences, University of Padova, Padova, Italy

ARTICLE INFO

Keywords:
Single-cell analysis
Impedance spectroscopy
Microfluidics
Antimicrobial peptides (AMPs)

ABSTRACT

The dielectric properties of biological cells provide critical insights into cellular physiology and have long been exploited for label-free diagnostics. While traditional approaches relied on bulk tissue or suspension measurements, advances in microfabrication have enabled single-cell electrical characterization, revealing subtle heterogeneities essential for precision medicine. Building on recent progress in single-cell impedance spectroscopy, we present a novel microfluidic impedance-based platform capable of rapid dielectric characterization of flowing cells at fourteen simultaneous, logarithmically spaced frequencies between 250 kHz and 50 MHz, achieving an unprecedented resolution of 6.1 data points per decade. The system integrates two synchronized lock-in amplifiers and a tailored signal-processing algorithm to reconstruct high-resolution impedance spectra at a throughput of up to 40 spectra per second. We demonstrate the approach on red blood cells (RBCs) and yeast cells, both under native conditions and under stress. For RBCs, chemical stress induced by antimicrobial peptides (AMPs) DNS-PMAP23 and trichogin GA IV revealed distinct dielectric alterations, while yeast cells exhibited measurable changes under thermal stress. Thousands of spectra were acquired and fitted to physically grounded models, enabling extraction of intrinsic parameters such as membrane capacitance and intracellular conductivity, as well as cell size. This work demonstrates the feasibility of high-throughput, high-resolution impedance spectroscopy of single cells, opening avenues for advanced diagnostics and biotechnological applications.

1. Introduction

The dielectric properties of biological cells have been of interest for more than a century (cf. e.g. the reviews (Foster and Schwan, 1989; Markx and Davey, 1999; Pethig and Schmueser, 2012)). Understanding these properties is pivotal for life science research and underpins a wide range of label-free diagnostic applications and therapeutic technologies. While early studies focused on the dielectric properties of tissues or cell suspensions, the development of microfabrication technologies has created opportunities for electrical characterization at the single-cell level. Compared to bulk measurements, single-cell analysis enables the detection of subtle differences between individual cells, facilitating the identification of rare cell types or abnormal cells, which is critical for precision medicine applications.

Single-cell dielectric properties can be obtained by impedance spectroscopy, i.e., by measuring cell impedance as a function of frequency. This approach can be classified into two main categories depending on whether measurements are performed on trapped cells or cells in flow. In the former case, dielectrophoresis (DEP) and/or hydrodynamic forces have been widely used for cell trapping. For instance, Wang et al. (2011) designed a microwell structure that uses negative DEP to capture single cells and measured the electrical impedance of trapped HeLa and MCF-7 cells in the 11 kHz–101 kHz range, finding significant differences between the two cell lines. Zhu et al. (2014) used hydrodynamic forces to capture single yeast cells and monitor over time their impedance in the 10 kHz–10 MHz frequency range, demonstrating

---

* Corresponding author.
E-mail address: caselli@ing.uniroma2.it (F. Caselli).
[1] Equal contribution.

https://doi.org/10.1016/j.bios.2026.118757
Received 13 January 2026; Received in revised form 24 April 2026; Accepted 29 April 2026

the ability of the technique to monitor cell growth. El Hasni et al. (2017) developed a microfluidic device combining hydrodynamic trapping and impedance spectroscopy measurements of single oocytes with frequencies ranging from 10 kHz to a few MHz and used the platform to investigate the contribution of the zona pellucida to the measured spectra. In the absence of stringent temporal constraints, impedance spectra of trapped cells can be acquired with high frequency resolution through a frequency sweep. Those impedance spectra can then be fitted using a single- or multi-shell model to derive the cell size and the dielectric properties (i.e., conductivity and permittivity) of the different cellular structures. However, the cell throughput (i.e., the number of measured cells per unit time) is generally low because of the limited multiplexing capabilities of typical platforms.

To increase throughput, microfluidic impedance cytometry (MIC) has been proposed (Cheung et al., 2005; Honrado et al., 2021; Righetto et al., 2025). In MIC, suspended particles flow one-by-one through a microchannel with integrated microelectrodes, and the variation in channel impedance induced by the passage of each individual cell is measured. A cell throughput of a few hundred per second can be achieved. On the other hand, cells remain in the sensing region only for a fraction of a millisecond, ruling out the possibility of frequency sweeping. Therefore, to achieve a multi-frequency characterization, a superposition of AC voltages is applied to the electrodes. Rather than reconstructing an impedance spectrum, MIC typically samples only two or three discrete frequencies, often including a low frequency (~0.5 MHz) to assess cell volume and a higher frequency (1–5 MHz) to probe membrane capacitance. As a result, in such systems, cell characterization is based on a limited set of features given by the impedance amplitude and phase at each measured frequency and/or derived quantities like the electrical opacity (i.e., the ratio of impedance amplitude at a high frequency to that at a low frequency). Such characterization proved to be effective for specific applications, including, e.g., monitoring cell viability (De Ninno et al., 2020; Zhong et al., 2022) and cell response to drugs (Chang et al., 2025; Spencer et al., 2020; Tang et al., 2023; Troiano et al., 2023) or discriminating among cell types (de Bruijn et al., 2021; He et al., 2024; Jarmoshti et al., 2025; Zhu et al., 2024, 2026). However, it fails to capture the complete frequency-dependent electrical behaviour of individual cells. The frequency range and resolution of those measurements are insufficient for accurate dielectric modelling, which requires fitting frequency-dependent impedance spectra to physically grounded models (e.g., single-shell or multi-shell formulations) to extract intrinsic parameters such as membrane capacitance, intracellular conductivity, and radius.

To perform multi-frequency single-cell impedance measurements in a short time, an approach using maximum length sequences (MLS) for periodic excitation signal was proposed (Sun et al., 2007), enabling 512 discrete frequencies in 1 ms. However, the bandwidth was limited to 500 kHz. Alternatively, population-based impedance spectra were built (Honrado et al., 2018; McGrath et al., 2019), which, however, miss the benefits of single-cell resolution.

Recently, Morgan's group took a seminal step toward overcoming the long-standing trade-off between high frequency resolution and high throughput in single-cell impedance spectroscopy (Spencer and Morgan, 2020). They introduced a high-speed single-cell characterization method that performs multi-frequency impedance measurements at eight simultaneous, logarithmically spaced frequencies between 250 kHz and 50 MHz, corresponding to a frequency resolution of about 3.5 data points per decade (i.e., $N/log_{10}(f_2/f_1)$, with $N=8$, $f_1=250$ kHz, $f_2=50$ MHz). That approach enabled the determination of intrinsic electrical properties of thousands of single cells at high throughput. Its applicability was demonstrated on red blood cells (RBCs) and red cell ghosts suspended in PBS, alongside reference beads. For each cell, the impedance spectrum was fitted to a single-shell dielectric model, yielding membrane capacitance, cytoplasm conductivity, cytoplasm permittivity, and radius. In a subsequent work (Zou et al., 2025), they distributed the eight frequencies over an extended frequency range (250 kHz–550 MHz, about 2.4 data points per decade), enabling the dielectric characterization of nucleated mammalian cells based on the double-shell model.

Building on Morgan's work (Spencer and Morgan, 2020; Zou et al., 2025), here we demonstrate for the first time fast impedance spectroscopy of single flowing cells at fourteen simultaneous frequencies between 250 kHz and 50 MHz, achieving an unprecedented frequency resolution (6.1 data points per decade). As detailed in Section 2, our system includes two sequential measurement zones, each connected to a lock-in amplifier. The two lock-in amplifiers use distinct frequency sets to characterize cell impedance and operate in a synchronized mode. The acquired signals are processed by a tailored algorithm to obtain a high-resolution impedance spectrum sampled at fourteen logarithmically spaced frequencies. We test the approach on two biologically relevant cell types: RBCs and yeast cells. Dielectric characterization of RBCs is particularly compelling, as it can reveal alterations associated with aging (e.g., storage lesions), disease (e.g., malaria infection), or external stressors (e.g., drug exposure). Similarly, the dielectric signatures of yeast cells vary during growth, division, and stress, making their monitoring valuable for applications in biotechnology, fermentation control, and cell-cycle analysis.

Here, as proof-of-concept applications, we present the dielectric characterization of RBCs and yeast cells in their native state and following exposure to a stressor. In the case of RBCs we investigate a chemical stress, namely exposure to antimicrobial peptides (AMPs). AMPs represent a promising class of compounds to combat antibiotic-resistant infections (Magana et al., 2020). They often kill bacteria and fungi by permeabilizing their cell membranes, thereby exhibiting a low propensity to induce resistance. However, the selectivity of AMPs for pathogens over host cells such as RBCs is essential (Savini et al., 2017). In this work, we consider two representative peptides: DNS-PMAP23, which perturbs cell membranes according to the so-called “carpet” mechanism, and trichogin GA IV, which follows a “barrel-stave-like” mechanism of action (Bobone et al., 2013; Roversi et al., 2014). For yeast cells, we consider a physical stress, namely prolonged exposure to high temperature.

The results of the analysis are reported in Section 3 and demonstrate the validity of the proposed approach for fast impedance spectroscopy of single flowing cells. Thousands of high-resolution single-cell spectra are acquired in a few minutes (i.e., at a throughput of up to 40 spectra per second) and fitted to physically grounded models. Moreover, significant alterations are observed in the spectra of treated versus native cells, both for RBCs and yeast cells, which reflect alterations of their dielectric properties. Current limitations of the proposed approach, as well as future perspectives, are discussed in Section 4.

2. Materials and methods

2.1. Working principle

The working principle of the proposed approach is summarized in Fig. 1. Individual flowing cells pass through the sensing region of the microfluidic chip, which comprises two measurement zones, denoted by A and B, respectively (Fig. 1(a–b)). Details of chip geometry and microfabrication are reported in Section S1 of the Supplementary Material and in the associated Fig. S1, which shows the main chip components: a polydimethylsiloxane (PDMS) block and a glass slide with patterned microelectrodes. In each measurement zone, a standard differential wiring scheme using three coplanar electrodes is employed: a multi-frequency voltage is applied to the central electrode, and the differential current flowing through the lateral electrodes is measured and demodulated by a lock-in amplifier. Distinct frequency sets are used by the two lock-in amplifiers, denoted by $\underline{\boldsymbol{f}}^{\boldsymbol{A}}$ and $\underline{\boldsymbol{f}}^{\boldsymbol{B}}$, respectively (Fig. 1(c)). For each measured cell, the impedance traces acquired from the two

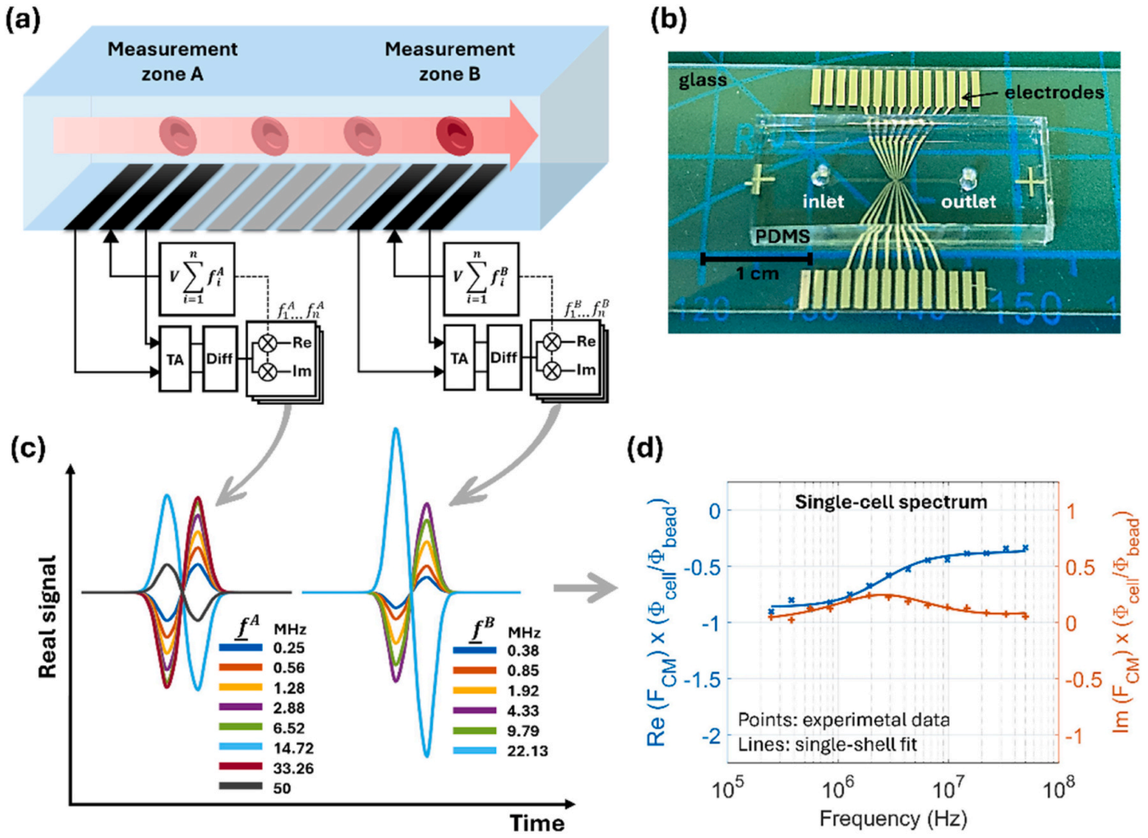

Fig. 1. Fast fourteen-frequency impedance spectroscopy of single flowing cells. (a) Schematic representation of the two consecutive measurement zones of the microfluidic chip, denoted A and B, respectively. Five floating electrodes (shown in grey) lie between the two zones. In each measurement zone, a multi-frequency voltage is applied to the central electrode, and the differential current collected from the two adjacent electrodes is demodulated using a lock-in amplifier (TA, transimpedance amplifier; Diff, differential amplifier; Re, real component; Im, imaginary component). (b) Photograph of the microfluidic chip. (c) Example of the signals (real part) generated by the passage of an erythrocyte (the bipolar Gaussian fit of the raw signals is shown). Overall, fourteen demodulated signals at logarithmically spaced frequencies ranging from 0.25 MHz to 50 MHz are collected (i.e., 6.1 data points per decade). Eight traces pertain to measurement zone A and six traces to measurement zone B. The latter traces are slightly delayed in time, consistent with the chip geometry. (d) Experimental impedance spectrum – i.e., real (Re) and imaginary (Im) parts of the cell Clausius-Mossotti factor F_{CM} multiplied by the ratio between cell and bead volume fractions Φ^{cell}/Φ^{bead}, as a function of frequency – along with its fit.

measurement zones are processed by a tailored algorithm. The signals from the two lock-in amplifiers are paired by estimating particle velocity from the signals collected in one measurement zone and using this estimate to compute the time at which the particle will be in the centre of the other measurement zone. Technical details are reported in Section S2 of the Supplementary Material and in the associated Fig. S2 (examples of raw signal traces) and Fig. S3 (bipolar Gaussian template used to fit the raw signals). From the measured impedance traces at 14 frequencies in the range 0.25–50 MHz, the experimental impedance spectrum is obtained and calibrated against reference beads to remove system nonlinearities (see Section S3 of the Supplementary Material). This experimental spectrum is then fitted with an appropriate shell model to obtain the cell dielectric properties (Fig. 1(d)). Shell models are described in Section S4 of the Supplementary Material and in the associated Fig. S4 (schematic of shell models) and Table S1 (collection of model parameters), whereas a sensitivity analysis for the parameters of the single-shell model is reported in Fig. S5 (Section S5 of the Supplementary Material).

2.2. AMPs

PMAP-23 is a 23-residue linear amphipathic peptide exhibiting broad-spectrum antimicrobial activity. The peptide exerts its action by compromising membrane integrity through a "carpet" mechanism, whereby PMAP-23 molecules accumulate on the lipid bilayer surface, altering membrane surface tension and inducing defect formation. Prof. Stella's group used a fluorescently labelled analogue of PMAP-23 (indicated as DNS-PMAP23, due to the presence of a dansyl label at the N-terminus) to quantitatively characterize its interaction with bacterial cell membranes (Roversi et al., 2014; Savini et al., 2020). In our recent study (Troiano et al., 2023), we showed that DNS-PMAP23 has significant haemolytic activity (i.e., 50% haemolysis at 0.15 μM for RBCs at 3×10^5 cells/mL), in agreement with previous literature. Furthermore, we demonstrated that the electrical signatures of human RBCs reflect this cytotoxic action (i.e., 50% RBC killing at 0.17 μM, for RBCs at 3×10^5 cells/mL).

Trichogin GA IV is an 11-residue amphipathic peptide with helical structure. Despite its short length, when a peptide/lipid threshold ratio is reached, it inserts into the cell membrane and forms pores according to the "barrel-stave" model (Bobone et al., 2013). Membrane thinning facilitates its spanning of the bilayer. In its native form, the peptide exhibits low haemolytic activity. Toniolo et al. (1996) reported a threshold effect for a concentration around 16 μM for RBCs at 10^7 cells/mL. This threshold is expected to decrease when RBCs are tested at lower cell densities (Savini et al., 2017).

DNS-PMAP23 was purchased from AnyGen Co. (Gwangju, South Korea). Trichogin GA IV was synthesized at the University of Padua, according to a previously published protocol (De Zotti et al., 2012).

2.3. Sample preparation

Blood was obtained from a healthy volunteer by finger prick, following the protocol for capillary sampling recommended by the World Health Organization (Dhingra, 2010). Informed consent was acquired from the sample donor. All the experiments were performed in accordance with relevant regulations and guidelines. The research was approved by the Independent Ethics Committee of the Tor Vergata University Hospital (protocol n. 2570).

A 5 μL droplet of capillary blood was diluted in a saline buffer (5 mM HEPES, pH = 7.3, 110 mM KCl, 15 mM glucose) to achieve a concentration of about 10^6 RBC/mL. Buffer conductivity was measured using a conductivity meter (Cond7, XS Instruments) and was found to be 0.996 S/m. In addition to native RBCs, RBCs exposed to AMPs were investigated. Peptide concentrations inducing significant cell damage were selected. Specifically, RBCs were incubated with either 1 μM DNS-PMAP23 or 20 μM trichogin GA IV for 30 min at 37 °C. Distinct capillary blood samples collected from the same donor were used in the experiments.

Baker's yeast (*Saccharomyces cerevisiae*) was obtained from a local grocery store and diluted in buffer to a final concentration of about 10^6 cells/mL. To mitigate yeast sedimentation, buffer density was increased by adding 13% (w/v) sucrose. The resulting buffer conductivity was 0.733 S/m. The yeast suspension was filtered using 10 μm CellTrics filters to remove possible cell clusters. An aliquot of the yeast suspension was then placed in an ultrasonic bath at 70 °C for 30 min, thereby inducing significant cell damage, as confirmed by Methylene Blue staining (see Section S6 of the Supplementary Material and the associated Fig. S6, which shows representative images of the staining assay).

Before the measurements, the samples were spiked with polystyrene beads (4.5 μm diameter) at a concentration of 2×10^5 beads/mL, to be used as an internal reference for impedance signal calibration. The cell suspensions were loaded into a 250 μL glass syringe and delivered to the microfluidic chip using a syringe pump (Harvard Apparatus) operating at 4 μL/min. Teflon tubing (200 μm internal diameter) was used to connect the syringe outlet to the microfluidic chip inlet. In a subset of experiments, the sample flowing through the sensing region was imaged using a high-speed video microscopy system (Photron Mini UX100, frame rate 4000 fps, shutter time 3.9 μs; Zeiss Axio Observer microscope with 20 × objective) simultaneously with the impedance measurements.

2.4. Initial assessment and optimization of the proposed approach

We performed preliminary experimental sessions aimed at optimizing the system configuration and verifying that the reconstructed impedance spectra are not biased by zone-specific transfer functions. A summary of this activity is reported in Section S7 of the Supplementary Material and in the associated Fig. S7 (showing the behaviour of bead signals across the 14 frequencies, for both devices). Moreover, we investigated cell motion through the sensing region, with a twofold aim: (i) analysing cell velocities and transit times and their influence on the signal processing algorithm, (ii) verifying that cells travel one-at-a-time and maintain rather stable trajectories, shape, and electrical signatures across the two measuring zones. The results are reported in Section S8 of the Supplementary Material and in the associated Fig. S8 (distribution of particle velocities and transit times) and Fig. S9 (representative examples of RBCs traveling through the sensing region).

3. Results

3.1. RBC analysis

Gating of RBC and bead populations was performed based on two features: the electrical phase (i.e., the phase of the complex peak amplitude) and the electrical diameter (i.e., the cube root of the modulus of the complex peak amplitude, multiplied by a calibration factor). Specifically, the electrical phase at 33.26 MHz and the electrical diameter at 1.28 MHz were selected, allowing a clear separation of the populations (Fig. 2(a, c, e)). In the control sample (panel (a)), the bead and RBC populations are close to each other, with RBCs exhibiting smaller phase and larger diameters on average. This characterization agrees with our previous work (Troiano et al., 2023). Furthermore, the identification of the RBC and bead populations was validated by analysing a synchronized video.

In the sample exposed to 1 μM DNS-PMAP23 (panel (c)), the RBC population shifts to smaller phases and larger diameters compared to the control sample. The decrease in phase after DNS-PMAP23 exposure is consistent with our previous findings (Troiano et al., 2023) (cf. also Fig. S10 of the Supplementary Material). Moreover, as in Ref. (Troiano et al., 2023), the treated RBC population was not visible with the adopted optical setup. Analysis of the sample exposed to 20 μM trichogin GA IV (panel (e)) revealed two RBC subpopulations: one subpopulation exhibits electrical features similar to the RBC population in the control sample and is visible in the video frames; the other subpopulation shows a broader distribution, characterized by smaller phase and smaller diameters on average, and was not visible in the video frames. This observation likely reflects the heterogeneous nature of peptide-membrane interactions (cf. Section S9 of the Supplementary Material). For comparison, additional results relevant to 1 μM trichogin GA IV are reported in Fig. S11 of the Supplementary Material, showing only one RBC population, with electrical features like those of native RBCs and optically visible.

The experimental impedance spectra of RBCs in the control sample, in the sample exposed to 1 μM DNS-PMAP23, and in the sample exposed to 20 μM trichogin GA IV (invisible subpopulation) are shown in Fig. 2 (b, d, f), respectively. Specifically, the median values and interquartile ranges (frequency by frequency) of the real and imaginary components of the Clausius-Mossotti factor F_{CM}^{cell} multiplied by the cell-to-bead volume ratio $\left(\Phi^{cell}/\Phi^{bead}\right)$ are reported (cf. eq. (5) of the Supplementary Material), along with the single-shell fit of the median values. In each case, thousands of single-RBC spectra are considered. Examples of single-RBC spectra are shown in Fig. 3(a–c). The median values and interquartile ranges of the fitted model parameters – i.e., the radius r, the membrane capacitance C_{mem}, and the cytoplasm conductivity σ_{cyt} – are summarized in Table 1. Additional details are provided in Section S10 of the Supplementary Material, namely: effect of fixed/free G_{mem} (Table S2), distribution of fit error (Fig. S12), nonparametric statistical analysis (Kruskal–Wallis and Mann–Whitney U tests), pairwise correlations among parameters (Table S3), and Cliff's delta values (Table S4). The scatter plots of the fitted parameters are shown in Fig. 3 (d–f), which highlights distinct alterations induced by DNS-PMAP23 and trichogin GA IV. Control RBCs are characterized by (median values): 2.7 μm radius, 0.95 $\mu F/cm^2$ membrane capacitance, and 0.41 S/m cytoplasm conductivity. These values are consistent with previous reports (Salahi et al., 2022; Spencer and Morgan, 2020). Incubation with DNS-PMAP23 and with trichogin GA IV is associated with larger (3.1 μm) and smaller (1.9 μm) median radius, respectively. Both peptides induce a reduction in membrane capacitance and an increase in cytoplasm conductivity. The former effect is comparable for both peptides (49% and 41% reduction in median C_{mem}, respectively), whereas the latter is more pronounced after exposure to DNS-PMAP23 (130% versus 100% increase in median σ_{cyt}), which also shows a narrower distribution.

3.2. Yeast analysis

Control and heat-treated yeasts were obtained from the same original suspension. For the control sample, gating of yeast and bead populations was implemented based on the electrical phase at 22.13 MHz and the electrical diameter at 6.52 MHz (Fig. 4(a)). In fact, at 22.13 MHz yeast

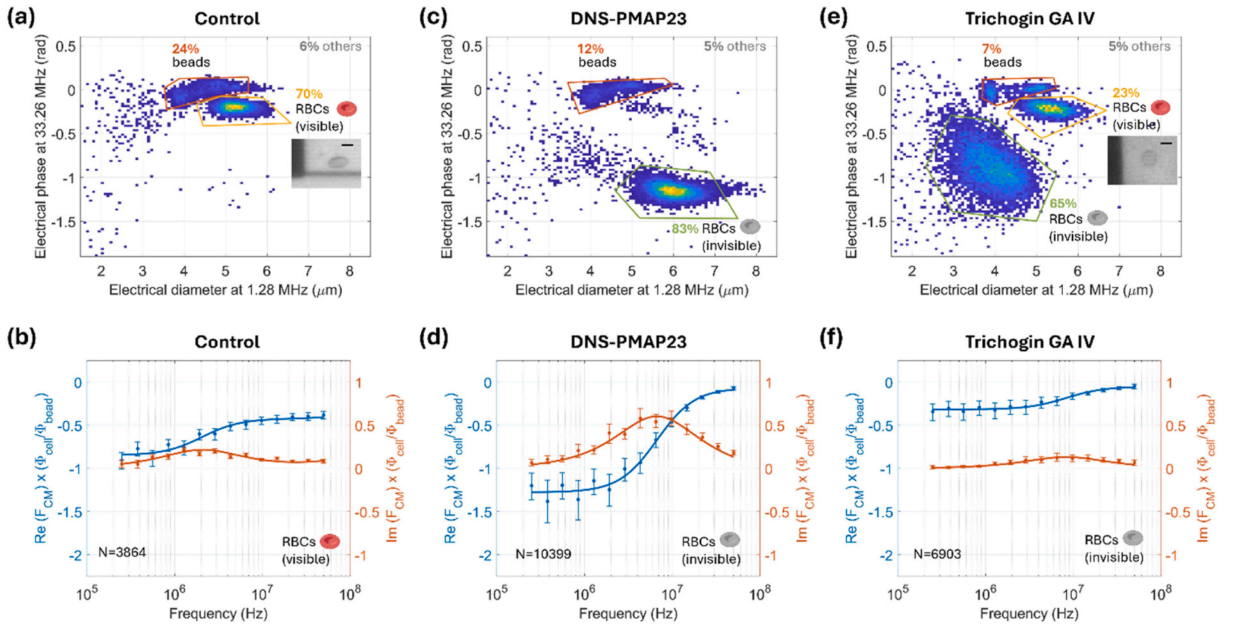

Fig. 2. Results of RBC measurements. (a, c, e) Electrical phase at 33.26 MHz versus electrical diameter at 1.28 MHz (control, 1 µM DNS-PMAP23, 20 µM trichogin GA IV, respectively). Median bead phase has been set to 0 for normalization. Gating and relative fractions of subpopulations are indicated. In (a) and (e), a representative image of a flowing RBC is also shown (5 µm scale bar). (b, d, f) Median values and interquartile ranges (frequency by frequency) of the real and imaginary components of the impedance spectrum, along with the single-shell fit of the median values (N, number of measured single-cell spectra).

cells exhibit a smaller phase than the calibration beads. For the heat-treated sample, population gating based on electrical features was not feasible. Heat treatment permeabilizes the cell membrane, thereby altering its Maxwell–Wagner polarization. Consequently, the electrical phase of the yeasts overlapped with that of the beads across all tested frequencies. Heat-treated yeasts and beads were manually labelled by visual inspection of associated video frames (Fig. 4(c)). Details of the labelling procedure are provided in Section S11 of the Supplementary Material and in the associated Fig. S13, which includes representative examples of the images shown to the annotator for classification.

The experimental impedance spectra of yeast cells in the control sample and in the heat-treated sample are shown in Fig. 4(b) and (d), respectively. Specifically, the median values and interquartile ranges, on a frequency-by-frequency basis, of the real and imaginary components of $F_{CM}^{cell}(\Phi^{cell}/\Phi^{bead})$ are reported. While the control sample exhibits a typical relaxation behaviour, the spectrum of heat-treated cells is almost constant across the frequency range. Accordingly, the fit of the median values based on the two-shell model is reported in panel (b), whereas a constant fit is shown in panel (d). Examples of single-yeast spectra are shown in Fig. S14 (Section S12 of the Supplementary Material).

For the control sample, the statistics of the fitted model parameters - i.e., the radius r, the membrane capacitance C_{mem}, and the intracellular conductivity σ_{int} - are summarized in Table 2. For some yeast cells, a slight discrepancy between the experimental data and their fit is noticeable at high frequency in the imaginary part, which can be reduced by setting the intracellular permittivity (ε_{int}) free in the fitting procedure (cf. dotted lines in Fig. 4(b) and Fig. S14(a)). The median value and interquartile range of ε_{int} were 81 ε_0 and [56 ε_0-110 ε_0], respectively, while the other model parameters remained stable (ε_0, vacuum permittivity). However, we note that an accurate determination of ε_{int} would require an extended frequency range.

For the heat-treated sample, the mean value across all the tested frequencies of the median values of $F_{CM}^{cell}(\Phi^{cell}/\Phi^{bead})$ was $-0.28+i0.03$. Heating induces coagulation of intracellular content with consequent decrease in intracellular conductivity. Assuming an intracellular conductivity of 0.05 S/m (Bunthawin et al., 2023), considering the medium conductivity of 0.73 S/m and neglecting permittivities, F_{CM}^{cell} turns out to be about -0.45. Accordingly, the estimated median radius of the heat-treated yeasts is about $r^{bead}\cdot\sqrt[3]{0.28/0.45} = 1.92$ µm. However, this should be regarded as a phenomenological descriptor specific to the present setup and assumptions.

4. Discussion

In this work, we demonstrated for the first time fourteen-frequency impedance spectroscopy of single cells at a throughput of up to 40 spectra per second (cf. also Fig. S15 in Section S13 of the Supplementary Material). This enabled the acquisition of thousands of single-cell spectra within a few minutes, with an unprecedented frequency resolution of 6.1 data points per decade. As proof-of-concept applications, the technique was applied to RBCs and yeast cells, native and under stress. Significant alterations in the dielectric properties of treated versus native cells were observed. A comparison between the present work and other relevant studies in the literature is provided in Table S5 (Section S14 of the Supplementary Material).

Several improvements can be envisaged for the proposed system. In this work, we used a microfluidic impedance chip with coplanar electrodes, which are straightforward to realize compared to facing electrodes that pose additional challenges in terms of fabrication and alignment. On the other hand, in coplanar electrode designs the electric field is less uniform, leading to a more pronounced position-induced blurring of the measured signals (Daguerre et al., 2020). This effect introduces an additional source of variability in the fitted cell dielectric parameters, beyond intrinsic cellular heterogeneity. Using facing-electrode designs with appropriate wiring schemes (e.g., Refs. (Caselli et al., 2018; Spencer and Morgan, 2020)) could mitigate this positional dependence, improving measurement accuracy at the expense

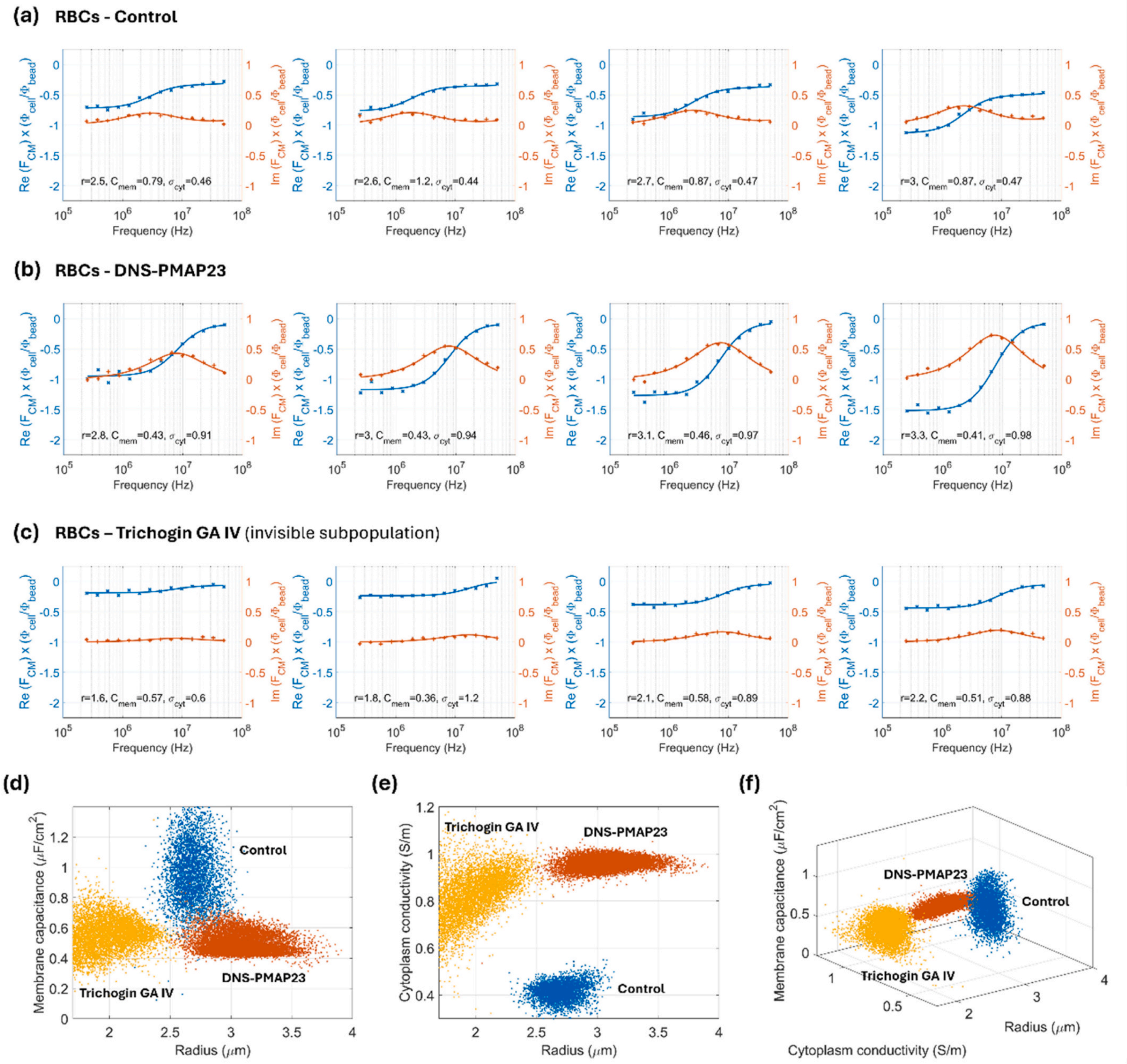

Fig. 3. (a-c) Fourteen-frequency impedance spectra of single RBCs. Four examples for each experimental condition are shown: (a) control, (b) 1 μM DNS-PMAP23, and (c) 20 μM trichogin GA IV (subpopulation of invisible RBCs). Data points denote the experimental measurements, while solid lines denote their fit. Fitted model parameters are also indicated (r, radius in μm; C_{mem}, membrane capacitance in μF/cm^2; σ_{cyt}, cytoplasm conductivity in S/m). (d-f) Scatter plots of the fitted single-RBC properties (control, blue; 1 μM DNS-PMAP23, red; 20 μM trichogin GA IV, yellow). (d) Membrane capacitance versus radius, (e) cytoplasm conductivity versus radius, and (f) 3D scatter plot. (For interpretation of the references to colour in this figure legend, the reader is referred to the Web version of this article.)

of a more complex fabrication process. In addition, the conductivity of the suspension medium could be further optimized to enhance the contrast between different cell phenotypes (Zou et al., 2025).

Because of hardware limitations, the frequency range investigated in this study was 0.25–50 MHz. Although the 50 MHz upper limit is sufficient to fit RBC data with a single-shell model, it is inadequate to fully characterize the electrical properties of nucleated mammalian cells suspended in physiological saline. For those applications, frequencies up to 550 MHz are required, as recently demonstrated by Zou et al. (2025) for native and treated HL60 cells and for THP-1 cells differentiated into macrophages. Achieving this extended range requires suitable high-frequency lock-in amplifiers (e.g., the UHFLI from Zurich Instruments, which covers DC to 600 MHz).

In the present system, the acquisition throughput is limited by the readout rate of the lock-in amplifiers, which – when recording eight channels simultaneously – cannot be increased beyond 28.8 kHz without data loss, thereby constraining the maximum particle velocity. Higher throughput could be achieved by increasing the sample concentration,

Table 1
Summary of fits for RBC measurements. For each experimental condition, the median values and interquartile ranges of the single-cell fits are reported (N, number of single-cell spectra), together with the fit of the median spectrum.

Sample	N	Radius ***r*** (μm)	Membrane capacitance C_{mem} (μF/cm^2)	Cytoplasm conductivity σ_{cyt} (S/m)
Control	3864	2.7 [2.6-2.8]	0.95 [0.81-1.1]	0.41 [0.39-0.44]
Control – median spectrum	-	2.7	0.97	0.41
DNS-PMAP23 (1 μM)	10399	3.1 [2.9-3.2]	0.48 [0.44-0.53]	0.96 [0.94-0.98]
DNS-PMAP23 (1 μM) – median spectrum	-	3.1	0.49	0.96
Trichogin GA IV (20 μM)	6903	1.9 [1.8-2.1]	0.56 [0.48-0.63]	0.82 [0.74-0.89]
Trichogin GA IV (20 μM) – median spectrum	-	1.9	0.55	0.81

but this would raise the probability of coincident events (Caselli et al., 2020). The acquired signals were processed offline, with correlation-based approaches for event detection and multichannel feature extraction. Alternatively, neural networks could be developed to enable real-time processing (Caselli et al., 2022), although this approach faces challenges related to potential fragility.

From an application standpoint, future work will focus on monitoring alterations in cell dielectric properties as a function of stressor intensity, as well as tracking their time dynamics. For instance, we hypothesize that the fraction of RBCs with altered dielectric properties will correlate with AMP concentration. Moreover, we expect that the dielectric properties of RBCs with peptide-induced membrane permeabilization will change over time, due to progressive exchange of material through the membrane defects or pores. In addition, biophysical studies will be pursued to elucidate the link between the measured electrical phenotypes and the structural cell alterations induced by AMPs. Depending on defect/pore size, selectivity, density, opening kinetics, and lifetime, as well as the properties of the suspension medium, defect/pore formation can produce either cell swelling or shrinkage. Our data — an increased radius for DNS-PMAP23 and a decreased radius for trichogin GA IV — are consistent with a swelling and a shrinking response, respectively. Both responses could be associated with an increase in measured intracellular conductivity, depending on the

Table 2
Summary of fits for yeast measurements. The median values and interquartile ranges of the single-cell fits are reported (N, number of single-cell spectra), together with the fit of the median spectrum.

Sample	N	Radius ***r*** (μm)	Membrane capacitance C_{mem} (μF/cm^2)	Intracellular conductivity σ_{int} (S/m)
Control	4558	2.5 [2.2-2.9]	0.55 [0.33-0.83]	0.68 [0.58-0.76]
Control – median spectrum	-	2.5	0.52	0.63

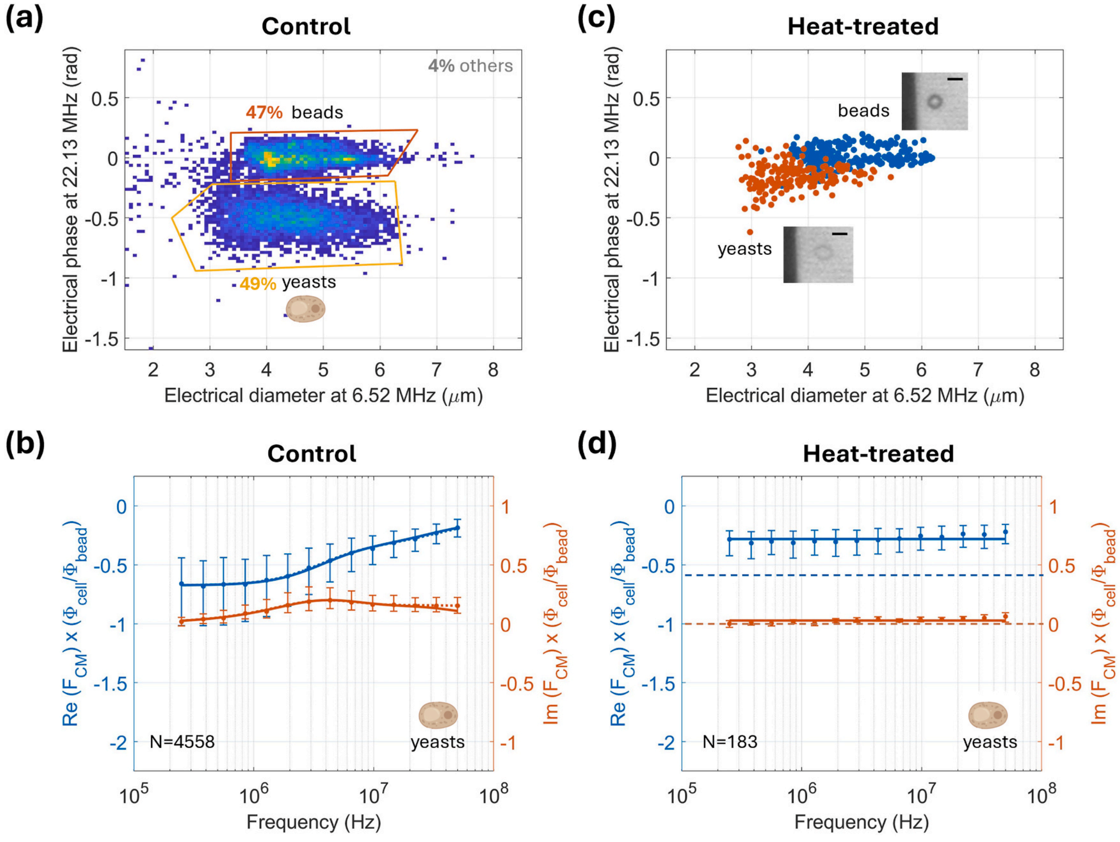

Fig. 4. Results of yeast measurements. (a, c) Electrical phase at 22.13 MHz versus electrical diameter at 6.52 MHz (control and heat treatment, respectively). In (c), representative images of a yeast and a bead are also shown (5 μm scale bars). (b, d) Median values and interquartile ranges (frequency by frequency) of the real and imaginary components of the impedance spectrum. In (b), the fit of the median values based on the two-shell model is also reported (solid/dotted lines indicate fits with ε_{int} fixed/free, respectively). In (d), a constant fit is shown as solid lines, while dashed lines indicate bead reference values.

direction and magnitude of material exchange. Further experiments are required to confirm this interpretation and to clarify how each peptide's mechanism of action produces the observed biophysical changes.

Beyond AMP studies, other application scenarios include monitoring changes in dielectric properties of RBCs associated with malaria infection, prolonged storage, or microgravity, and yeast viability monitoring for fermentation process control.

CRediT authorship contribution statement

Marta Righetto: Investigation, Methodology, Visualization, Writing – original draft, Writing – review & editing. **Riccardo Reale:** Funding acquisition, Investigation, Methodology, Supervision, Writing – review & editing. **Federico Carneri:** Methodology, Writing – review & editing. **Alessandra Mistretta:** Investigation, Writing – review & editing. **Marta De Zotti:** Funding acquisition, Resources, Writing – review & editing. **Daniela Roversi:** Methodology, Resources, Writing – review & editing. **Paolo Bisegna:** Investigation, Methodology, Software, Writing – review & editing. **Adele De Ninno:** Funding acquisition, Investigation, Methodology, Resources, Supervision, Writing – review & editing. **Federica Caselli:** Conceptualization, Formal analysis, Funding acquisition, Investigation, Methodology, Project administration, Resources, Software, Supervision, Visualization, Writing – original draft, Writing – review & editing.

Declaration of competing interest

The authors declare that they have no known competing financial interests or personal relationships that could have appeared to influence the work reported in this paper.

Acknowledgments

This work is dedicated to the memory of our beloved colleague and friend, Lorenzo Stella. This research was funded by the European Union – Next Generation EU, Mission 4, Component 1 – CUP E53D23002530006 (grant 2022245PTX) and by the University of Rome Tor Vergata (grant NN4RTA_RSA_2024). M. D. Z. thanks the University of Padova for funding (pDisc project no. DEZO_BIRD23_01).

Appendix A. Supplementary data

Supplementary data to this article can be found online at https://doi.org/10.1016/j.bios.2026.118757.

Data availability

Data will be made available on request.

References

Bobone, S., Gerelli, Y., De Zotti, M., Bocchinfuso, G., Farrotti, A., Orioni, B., Sebastiani, F., Latter, E., Penfold, J., Senesi, R., Formaggio, F., Palleschi, A., Toniolo, C., Fragneto, G., Stella, L., 2013. Membrane thickness and the mechanism of action of the short peptaibol trichogin GA IV. Biochim. Biophys. Acta Biomembr. 1828. https://doi.org/10.1016/j.bbamem.2012.11.033.

Bunthawin, S., Srichan, P., Jaruwongrungsee, K., Ritchie, R.J., 2023. Using dielectrophoretic spectra to identify and separate viable yeast cells. Appl. Microbiol. Biotechnol. 107. https://doi.org/10.1007/s00253-023-12809-5.

Caselli, F., De Ninno, A., Reale, R., Businaro, L., Bisegna, P., 2020. A Bayesian approach for coincidence resolution in microfluidic impedance cytometry. IEEE Trans. Biomed. Eng. 68, 340–349. https://doi.org/10.1109/TBME.2020.2995364.

Caselli, F., Ninno, A. De, Reale, R., Businaro, L., Bisegna, P., 2018. A novel wiring scheme for standard chips enabling high-accuracy impedance cytometry. Sens. Actuators, B Chem. 256, 580–589. https://doi.org/10.1016/j.snb.2017.10.113.

Caselli, F., Reale, R., De Ninno, A., Spencer, D., Morgan, H., Bisegna, P., 2022. Deciphering impedance cytometry signals with neural networks. Lab Chip 22, 1714–1722. https://doi.org/10.1039/D2LC00028H.

Chang, Y., Zhong, J., Bin Kassim, A.K., Koo, S.H., Tan, T.Y., Zhou, Y., Ai, Y., 2025. Comprehensive evaluation of clinical antimicrobial resistance using impedance-accelerated single-bacterium multiplex screening strategy. Sens. Actuators, B Chem. 423, 136764. https://doi.org/10.1016/j.snb.2024.136764.

Cheung, K., Gawad, S., Renaud, P., 2005. Impedance spectroscopy flow cytometry: on-chip label-free cell differentiation. Cytometry A 65A, 124–132. https://doi.org/10.1002/cyto.a.20141.

Daguerre, H., Solsona, M., Cottet, J., Gauthier, M., Renaud, P., Bolopion, A., 2020. Positional dependence of particles and cells in microfluidic electrical impedance flow cytometry: origin, challenges and opportunities. Lab Chip 20, 3665–3689. https://doi.org/10.1039/d0lc00616e.

de Bruijn, D.S., ter Braak, P.M., Van de Waal, D.B., Olthuis, W., van den Berg, A., 2021. Coccolithophore calcification studied by single-cell impedance cytometry: towards single-cell PIC:POC measurements. Biosens. Bioelectron. 173, 112808. https://doi.org/10.1016/j.bios.2020.112808.

De Ninno, A., Reale, R., Giovinazzo, A., Bertani, F.R., Businaro, L., Bisegna, P., Matteucci, C., Caselli, F., 2020. High-throughput label-free characterization of viable, necrotic and apoptotic human lymphoma cells in a coplanar-electrode microfluidic impedance chip. Biosens. Bioelectron. 150, 111887. https://doi.org/10.1016/j.bios.2019.111887.

De Zotti, M., Biondi, B., Peggion, C., Formaggio, F., Park, Y., Hahm, K.S., Toniolo, C., 2012. Trichogin GA IV: a versatile template for the synthesis of novel peptaibiotics. Org. Biomol. Chem. 10. https://doi.org/10.1039/c1ob06178j.

Dhingra, N., 2010. WHO Guidelines on Drawing Blood: Best Practices in Phlebotomy. World Health Organization.

El Hasni, A., Schmitz, C., Bui-Göbbels, K., Bräunig, P., Jahnen-Dechent, W., Schnakenberg, U., 2017. Electrical impedance spectroscopy of single cells in hydrodynamic traps. Sens. Actuators, B Chem. 248. https://doi.org/10.1016/j.snb.2017.04.019.

Foster, K.R., Schwan, H.P., 1989. Dielectric properties of tissues and biological materials: a critical review. Crit. Rev. Biomed. Eng. 17, 25–104.

He, L., Tan, J., Ng, S.Y., Li, K.H.H., Han, J., Chew, S.Y., Hou, H.W., 2024. Label-free impedance analysis of induced pluripotent stem cell-derived spinal cord progenitor cells for rapid safety and efficacy profiling. Adv. Mater. Technol. 9, 2400589. https://doi.org/10.1002/admt.202400589.

Honrado, C., Bisegna, P., Swami, N.S., Caselli, F., 2021. Single-cell microfluidic impedance cytometry: from raw signals to cell phenotypes using data analytics. Lab Chip 21, 22–54. https://doi.org/10.1039/D0LC00840K.

Honrado, C., Ciuffreda, L., Spencer, D., Ranford-Cartwright, L., Morgan, H., 2018. Dielectric characterization of Plasmodium falciparum-infected red blood cells using microfluidic impedance cytometry. J. R. Soc. Interface 15. https://doi.org/10.1098/rsif.2018.0416.

Jarmoshti, J., Siddique, A.-B., Xu, P., Başlık, A., Mirhosseini, S., Mai, S., Kadin, M.E., Swami, N.S., 2025. Multiparametric single-cell biophysical cytometry under tunable viscoelastic extensional flows for classification of T-cell lymphomas on their nuclear phenotypes. Biosens. Bioelectron. 289, 117879. https://doi.org/10.1016/j.bios.2025.117879.

Magana, M., Pushpanathan, M., Santos, A.L., Leanse, L., Fernandez, M., Ioannidis, A., Giulianotti, M.A., Apidianakis, Y., Bradfute, S., Ferguson, A.L., Cherkasov, A., Seleem, M.N., Pinilla, C., de la Fuente-Nunez, C., Lazaridis, T., Dai, T., Houghten, R. A., Hancock, R.E.W., Tegos, G.P., 2020. The value of antimicrobial peptides in the age of resistance. Lancet Infect. Dis. https://doi.org/10.1016/S1473-3099(20)30327-3.

Markx, G.H., Davey, C.L., 1999. The dielectric properties of biological cells at radiofrequencies: applications in biotechnology. Enzym. Microb. Technol. https://doi.org/10.1016/S0141-0229(99)00008-3.

McGrath, J.S., Honrado, C., Moore, J.H., Adair, S.J., Varhue, W.B., Salahi, A., Farmehini, V., Goudreau, B.J., Nagdas, S., Blais, E.M., Bauer, T.W., Swami, N.S., 2019. Electrophysiology-based stratification of pancreatic tumorigenicity by label-free single-cell impedance cytometry. Anal. Chim. Acta 1101, 90–98. https://doi.org/10.1016/j.aca.2019.12.033.

Pethig, R., Schmueser, I., 2012. Marking 100 years since Rudolf Höber's discovery of the insulating envelope surrounding cells and of the β-dispersion exhibited by tissue. J. Electr. Bioimpedance 3. https://doi.org/10.5617/jeb.401.

Righetto, M., Brandi, C., Reale, R., Caselli, F., 2025. Integrating impedance cytometry with other microfluidic tools towards multifunctional single-cell analysis platforms. Lab Chip 25, 1316–1341. https://doi.org/10.1039/D4LC00957F.

Roversi, D., Luca, V., Aureli, S., Park, Y., Mangoni, M.L., Stella, L., 2014. How many antimicrobial peptide molecules kill a bacterium? The case of PMAP-23. ACS Chem. Biol. 9. https://doi.org/10.1021/cb500426r.

Salahi, A., Honrado, C., Rane, A., Caselli, F., Swami, N.S., 2022. Modified red blood cells as multimodal standards for benchmarking single-cell cytometry and separation based on electrical physiology. Anal. Chem. 94, 2865–2872. https://doi.org/10.1021/acs.analchem.1c04739.

Savini, F., Loffredo, M.R., Troiano, C., Bobone, S., Malanovic, N., Eichmann, T.O., Caprio, L., Canale, V.C., Park, Y., Mangoni, M.L., Stella, L., 2020. Binding of an antimicrobial peptide to bacterial cells: interaction with different species, strains and cellular components. Biochim. Biophys. Acta Biomembr. 1862. https://doi.org/10.1016/j.bbamem.2020.183291.

Savini, F., Luca, V., Bocedi, A., Massoud, R., Park, Y., Mangoni, M.L., Stella, L., 2017. Cell-density dependence of host-defense peptide activity and selectivity in the presence of host cells. ACS Chem. Biol. 12. https://doi.org/10.1021/acschembio.6b00910.

Spencer, D.C., Paton, T.F., Mulroney, K.T., Inglis, T.J.J., Sutton, J.M., Morgan, H., 2020. A fast impedance-based antimicrobial susceptibility test. Nat. Commun. 11, 5328. https://doi.org/10.1038/s41467-020-18902-x.

Spencer, D., Morgan, H., 2020. High-speed single-cell dielectric spectroscopy. ACS Sens. 5, 423–430. https://doi.org/10.1021/acssensors.9b02119.

Sun, T., Gawad, S., Bernabini, C., Green, N.G., Morgan, H., 2007. Broadband single cell impedance spectroscopy using maximum length sequences: theoretical analysis and practical considerations. Meas. Sci. Technol. 18, 2859–2868. https://doi.org/10.1088/0957-0233/18/9/015.

Tang, T., Liu, X., Yuan, Y., Kiya, R., Zhang, T., Yang, Y., Suetsugu, S., Yamazaki, Y., Ota, N., Yamamoto, K., Kamikubo, H., Tanaka, Y., Li, M., Hosokawa, Y., Yalikun, Y., 2023. Machine learning-based impedance system for real-time recognition of antibiotic-susceptible bacteria with parallel cytometry. Sens. Actuators, B Chem. 374, 132698. https://doi.org/10.1016/j.snb.2022.132698.

Toniolo, C., Crisma, M., Formaggio, F., Peggion, C., Monaco, V., Goulard, C., Rebuffat, S., Bodo, B., 1996. Effect of Nα-acyl chain length on the membrane-modifying properties of synthetic analogs of the lipopeptaibol trichogin GA IV. J. Am. Chem. Soc. 118. https://doi.org/10.1021/ja954081o.

Troiano, C., De Ninno, A., Casciaro, B., Riccitelli, F., Park, Y., Businaro, L., Massoud, R., Mangoni, M.L., Bisegna, P., Stella, L., Caselli, F., 2023. Rapid assessment of susceptibility of bacteria and erythrocytes to antimicrobial peptides by single-cell impedance cytometry. ACS Sens. 8, 2572–2582. https://doi.org/10.1021/acssensors.3c00256.

Wang, M.H., Kao, M.F., Jang, L.S., 2011. Single HeLa and MCF-7 cell measurement using minimized impedance spectroscopy and microfluidic device. Rev. Sci. Instrum. 82. https://doi.org/10.1063/1.3594550.

Zhong, J., Li, P., Liang, M., Ai, Y., 2022. Label-free cell viability assay and enrichment of cryopreserved cells using microfluidic cytometry and on-demand sorting. Adv. Mater. Technol. 7, 2100906. https://doi.org/10.1002/admt.202100906.

Zhu, J., Pan, S., Chai, H., Zhao, P., Feng, Y., Cheng, Z., Zhang, S., Wang, W., 2024. Microfluidic impedance cytometry enabled one-step sample preparation for efficient single-cell mass spectrometry. Small 20, 2310700. https://doi.org/10.1002/smll.202310700.

Zhu, S., Zhou, Z., Xiang, N., Ni, Z., 2026. Microfluidic impedance cytometer with face-to-face electrodes for multi-parameter phenotyping and accurate discrimination of cells. Sens. Actuators, B Chem. 448, 138978. https://doi.org/10.1016/j.snb.2025.138978.

Zhu, Z., Frey, O., Franke, F., Haandbæk, N., Hierlemann, A., 2014. Real-time monitoring of immobilized single yeast cells through multifrequency electrical impedance spectroscopy. Anal. Bioanal. Chem. 406, 7015–7025. https://doi.org/10.1007/s00216-014-7955-9.

Zou, X., Spencer, D.C., Morgan, H., 2025. Single-cell impedance spectroscopy of nucleated cells. Lab Chip 25, 2939–2948. https://doi.org/10.1039/D5LC00111K.

Supplementary Material to:

Fast fourteen-frequency impedance spectroscopy of single erythrocytes and yeast cells in flow

Marta Righetto[§,a], Riccardo Reale[§,a], Federico Carneri[b], Alessandra Mistretta[c],
Marta De Zotti[d], Daniela Roversi[b], Paolo Bisegna[a], Adele De Ninno[c], Federica Caselli[*,a]

[a] *Department of Civil Engineering and Computer Science, University of Rome Tor Vergata, Rome, Italy*
[b] *Department of Chemical Science and Technologies, University of Rome Tor Vergata, Rome, Italy*
[c] *Institute for Photonics and Nanotechnology, Italian National Research Council, Rome, Italy*
[d] *Department of Chemical Sciences, University of Padova, Padova, Italy*
*(§ equal contribution, * corresponding author)*

Content:

S1. MICROFLUIDIC CHIP

The microfluidic chip (Fig. 1(b) of the main text) consists of a polydimethylsiloxane (PDMS) block housing the microchannel (Fig. S1(a)), bonded to a glass slide with patterned platinum (Pt) electrodes (Fig. S1(b)). In the sensing area, the microchannel is 40 µm wide and 10 µm high. A micropillar array is included in the fluidic layout on the inlet side to mitigate the risk of microchannel clogging.

PDMS microchannels were fabricated by replica moulding from microstructured silicon wafers patterned by photolithography using laminated epoxy-based ADEX10 dry film resist. Microelectrodes (15 µm width, 5 µm interelectrode spacing) were fabricated on glass substrates (75 mm × 25 mm) by optical photolithography, metal deposition, and lift-off. A bilayer resist (LOR 7B/S1813, ~1.3 µm) was spin-coated, exposed with an EVG10 mask aligner (150 mJ cm^{-2}), and developed in MF-319 to generate an undercut profile. Ti/Pt thin films (10/200 nm) were deposited by RF sputtering under Ar (60 sccm; Ti: 500 W; Pt: 200 W), followed by lift-off in Remover PG (30–60 min) to yield well-defined microelectrode arrays. PDMS layers and electrode-patterned glass substrates were treated with O_2 plasma in a reactive ion etcher (20 W RF power, 60 sccm O_2, ~800 mTorr, 30 s) and immediately aligned under an optical microscope to achieve irreversible bonding.

The microfluidic chip is inserted into a custom chip holder for electrical connection to the electronic acquisition system.

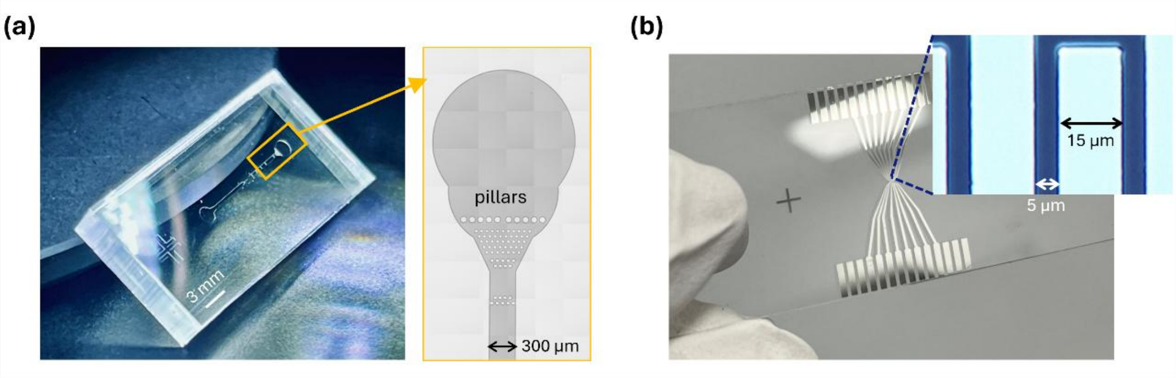

Fig. S1. (a) PDMS block housing the microfluidic channel, along with an illustration of the pillar layout near the fluidic inlet. (b) Picture of the glass slide with patterned microelectrodes, along with a microscopy image of representative electrodes of the sensing region (15 µm electrode width, 5 µm interelectrode spacing).

S2. IMPEDANCE DATA ACQUISITION AND PROCESSING

Two commercial lock-in amplifiers (Zurich Instruments) were used: the HF2IS, which allows a maximum of eight simultaneous frequencies, and the HF2LI, which allows a maximum of six. The frequency range of both amplifiers is 0–50 MHz. The devices were controlled via the LabOne® software (Zurich Instruments), which enables multi-device synchronization and allows users to access them through a single graphical user interface. Full synchronization includes stable and well-defined phase relationships between the various reference clocks and the alignment of time stamps and sampling rates for the recorded signals. Fourteen logarithmically spaced frequencies from 0.25 to 50 MHz were considered, i.e.: 0.25, 0.38, 0.56, 0.85, 1.28, 1.92, 2.88, 4.33, 6.52, 9.79, 14.72, 22.13, 33.26, and 50 MHz. These frequencies were distributed between the two lock-in amplifiers in an alternating pattern to maximize the frequency separation within each device. Specifically, the HF2IS applied a multi-frequency signal to the central electrode of measurement zone A, given by the superposition of sinusoidal voltages at 0.25, 0.56, 1.28, 2.88, 6.52, 14.72, 33.26, and 50 MHz (1.25 V each), while the HF2LI applied a multi-frequency signal to the central electrode of measurement zone B, given by the superposition of sinusoidal voltages at 0.38, 0.85, 1.92, 4.33, 9.79, and 22.13 MHz (1.25 V each). The electric currents collected from the lateral electrodes of each measurement zone were conditioned with a transimpedance amplifier (HF2TA, Zurich Instruments, 1 kΩ gain) and sent to the respective device as input for lock-in demodulation. For both devices, the readout rate was set to 28.8 kHz and the bandwidth to 14 kHz. Due to the adopted differential measurement scheme, in each frequency channel the event signals (i.e., the signal portions associated to the passage of a cell over the measurement zone) exhibited a characteristic bipolar shape.

We designed the experiment to guarantee a few thousand cells per sample. Assuming a concentration of 10^6 cell/mL and a flow rate of 4 µL/min, 4 thousand cells are recorded every minute. To compensate for a potential reduction in the effective cell concentration (e.g., due to cell sedimentation within the syringe or overestimates of the initial concentration), we set the recording time to 5 minutes.

A custom MATLAB toolkit was developed to construct the experimental single-cell impedance spectra by processing the demodulated impedance signals as described below (cf. also Fig. S2). First, the frequency channel with the best signal-to-noise ratio (SNR) is identified — it may originate from either measurement zone A or measurement zone B. Let us assume, for instance, that it is from measurement zone A. This channel is then used to perform event-detection (i.e., the detection of event signals in the data stream). For each detected event, the collection of traces from measurement zone A is fitted with a bipolar Gaussian template (Fig. S3), thereby yielding the complex peak amplitudes $\underline{\boldsymbol{a}}^{\boldsymbol{A}}$ at the corresponding frequencies $\underline{\boldsymbol{f}}^{\boldsymbol{A}}$. Moreover, an electrical estimate of cell velocity v is computed from the peak-to-peak time δ and the distance between peak positions ($L_{p2p} = 20$ µm), i.e., $v = L_{p2p}/\delta$. This velocity is then used to estimate the location of the event signal within the data stream from measurement zone B. Specifically, it will be delayed by $\Delta = L/v$ relative to measurement zone A, where $L = 160$ µm is the distance between the centres of the two measurement zones. Feature extraction on the collection of traces from measurement zone B is then carried out analogously, yielding the complex peak amplitudes $\underline{\boldsymbol{a}}^{\boldsymbol{B}}$ at the corresponding frequencies $\underline{\boldsymbol{f}}^{\boldsymbol{B}}$. In what follows, the complex peak amplitude at a generic frequency f will be denoted by S (selected from either $\underline{\boldsymbol{a}}^{\boldsymbol{A}}$ or $\underline{\boldsymbol{a}}^{\boldsymbol{B}}$, depending on whether f belongs to $\underline{\boldsymbol{f}}^{\boldsymbol{A}}$ or $\underline{\boldsymbol{f}}^{\boldsymbol{B}}$).

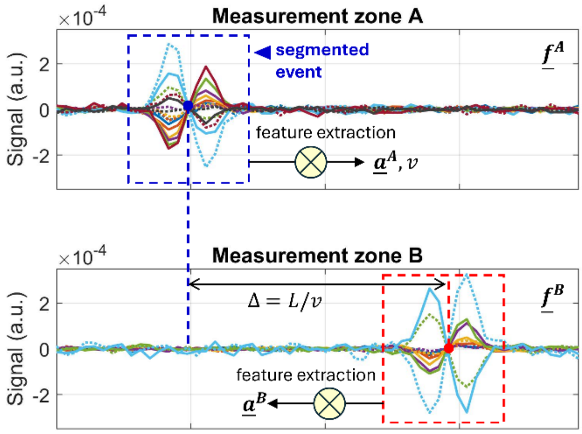

Fig. S2. Example of raw signal traces for a typical event (solid line, real parts; dotted lines, imaginary parts). The main processing steps are indicated: the event is first localized in measurement zone A using a segmentation algorithm; a correlation-based feature extraction is then performed on the associated traces, yielding the peak amplitudes $\underline{\boldsymbol{a}}^{\boldsymbol{A}}$ at the frequencies $\underline{\boldsymbol{f}}^{\boldsymbol{A}}$ as well as an estimate of the particle velocity v; this velocity is used to estimate the delay Δ, thereby localizing the event in measurement zone B; feature extraction is then performed on the associated traces, yielding the peak amplitudes $\underline{\boldsymbol{a}}^{\boldsymbol{B}}$ at the frequencies $\underline{\boldsymbol{f}}^{\boldsymbol{B}}$.

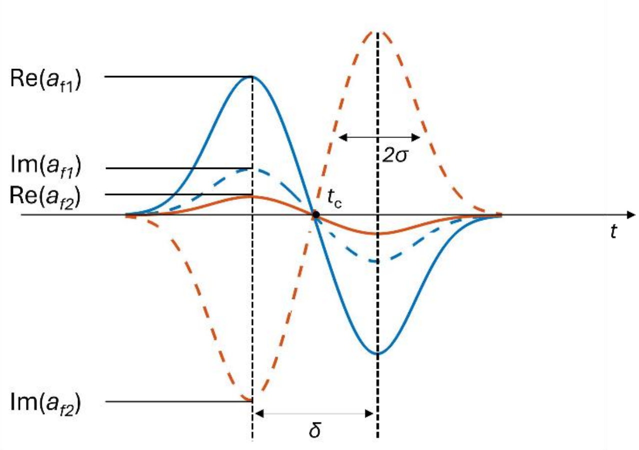

Fig. S3. Bipolar Gaussian template used to fit the single-cell events. The template is defined as:

$$s_f(t) = a_f\left(e^{-\frac{(t-(t_c-\delta/2))^2}{2\sigma^2}} - e^{-\frac{(t-(t_c+\delta/2))^2}{2\sigma^2}}\right) \qquad (1)$$

where a_f is the complex, frequency-dependent amplitude, σ is the peak-width control, δ is the peak-to-peak time, and t_c is the central time. For ease of illustration, only two frequencies (f_1 and f_2) are considered in the figure. In practice, multi-frequency templates including eight and six frequencies were used to fit the events from measurement zones A and B, respectively. The complex amplitude is used to build the impedance spectra. In addition, for population gating, the complex amplitude is converted into modulus and phase, on a frequency-by-frequency basis. Since the signal modulus is proportional to cell volume, its cube root is proportional to cell diameter (the electrical diameter).

S3. CALIBRATED IMPEDANCE SPECTRA

Polystyrene beads of known size and dielectric properties are used as internal calibration particles to compensate for possible system nonlinearities — as is customary in microfluidic impedance cytometry — and differences between the two measurement zones.

As fully detailed e.g. in the review (Honrado et al., 2021) (Section 3.2 and Scheme 2A), the measured signal S is given by:

$$S = H(\omega) I_{diff}, \qquad (2)$$

where $H(\omega)$ is the transfer function of the acquisition system and I_{diff} is the differential current collected from the electrodes. The latter current is proportional to the product $F_{CM}\Phi$, where Φ denotes the volume fraction (i.e., the ratio between the particle volume and the measurement-zone volume) and F_{CM} denotes the Clausius-Mossotti factor, which depends on the complex permittivities ($\tilde{\varepsilon}$) of the particle (either a cell or a bead) and the medium:

$$F_{CM} = \frac{\tilde{\varepsilon}_{particle} - \tilde{\varepsilon}_{med}}{\tilde{\varepsilon}_{particle} + 2\tilde{\varepsilon}_{med}}. \qquad (3)$$

Upon calibration, the complex peak amplitudes of cells (denoted by S^{cell}) are normalized with respect to the median value of the complex peak amplitudes of co-flowing beads (denoted by S^{bead}), resulting in:

$$\frac{S^{cell}}{S^{bead}} = \frac{F_{CM}^{cell}\Phi^{cell}}{F_{CM}^{bead}\Phi^{bead}} = \frac{F_{CM}^{cell}}{F_{CM}^{bead}}\left(\frac{r^{cell}}{r^{bead}}\right)^3, \qquad (4)$$

where r denotes the particle radius. This operation, performed frequency-by-frequency, effectively cancels out non-linearities of the measurement system across the $0.25-50$ MHz range.

According to eq. (4), the unknown cell Clausius-Mossotti factor (F_{CM}^{cell}), times Φ^{cell}/Φ^{bead}, can be obtained by multiplying the experimentally measured ratio S^{cell}/S^{bead} by the bead Clausius-Mossotti factor F_{CM}^{bead}:

$$F_{CM}^{cell}\frac{\Phi^{cell}}{\Phi^{bead}} = F_{CM}^{cell}\left(\frac{r^{cell}}{r^{bead}}\right)^3 = F_{CM}^{bead}\frac{S^{cell}}{S^{bead}} \qquad (5)$$

Here F_{CM}^{bead} and r^{bead}, corresponding to the calibration beads (modelled as homogeneous spheres), can be regarded as known quantities, whereas F_{CM}^{cell} and r^{cell} are to be determined.

By fitting an appropriate shell model (Cottet et al., 2019) to the above calibrated data, measured at multiple frequencies, the cell radius and the dielectric properties of the subcellular features that appear in the expression of F_{CM}^{cell} can be estimated. For erythrocytes, we used the single-shell model, in which the cell is characterized by the conductivity and permittivity of the intracellular space (i.e., the cytoplasm) and of the plasma membrane, treated as a thin shell. For yeast cells, an additional outer layer was considered, representing the cell wall (two-shell model). Unless otherwise stated, in both cases three parameters were fitted, namely the cell radius r, the membrane capacitance C_{mem}, and the intracellular conductivity σ_{int}. For erythrocytes, σ_{int} represents cytoplasm conductivity and is therefore denoted by σ_{cyt}. On the other hand, r is a spherical-equivalent descriptor given the nonsphericity of RBCs. Relevant details of the shell models are provided in Section S4.

S4. SHELL MODELS OF ERYTHROCYTES AND YEAST CELLS

As introduced in Section S3, the Clausius–Mossotti factor of a cell is given by:

$$F_{CM} = \frac{\tilde{\varepsilon}_{cell} - \tilde{\varepsilon}_{med}}{\tilde{\varepsilon}_{cell} + 2\tilde{\varepsilon}_{med}}, \quad (6)$$

where $\tilde{\varepsilon}_{med}$ is the complex permittivity of the suspending medium, written as:

$$\tilde{\varepsilon}_{med} = \varepsilon_{med} + \frac{\sigma_{med}}{j\omega} \quad (7)$$

with ε_{med} the (real) permittivity, σ_{med} the conductivity, ω the angular frequency, and $j = \sqrt{-1}$. The complex permittivity of the cell, $\tilde{\varepsilon}_{cell}$, is usually described using single- or multi-shell models (Cottet et al., 2019; Honrado et al., 2021). Shell models approximate each cell as a set of concentric spherical layers, each characterized by its own conductivity σ and permittivity ε.

In this work, erythrocytes are represented by a single-shell model, in which the intracellular compartment (i.e., the cytoplasm) is surrounded by a thin shell, corresponding to the plasma membrane (Fig. S4(a)). To simplify the model, a spherical geometry is assumed. For yeast cells, an additional outer (thick) shell is included, to account for the cell wall (Fig. S4(b)).

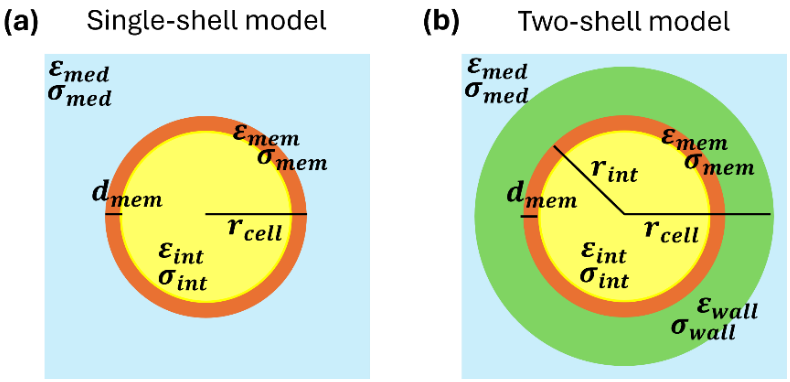

Fig. S4. (a) Single-shell model used for the electrical characterization of erythrocytes. (b) Two-shell model used for the electrical characterization of yeast cells. Subscripts: “med”, suspending medium; “mem”, membrane; “int”, intracellular compartment.

SINGLE-SHELL ERYTHROCYTE MODEL

According to the single-shell model, the effective complex permittivity of the cell, $\tilde{\varepsilon}_{cell}$, is given by (Honrado et al., 2021):

$$\tilde{\varepsilon}_{cell} = \tilde{\varepsilon}_{int}\frac{\chi}{1+\chi} \quad (8)$$

with:

$$\chi = \frac{\tilde{\varepsilon}_{mem}/d_{mem}}{\tilde{\varepsilon}_{int}/r_{cell}}, \quad (9)$$

and the complex permittivities of the membrane and intracellular compartment are:

$$\tilde{\varepsilon}_{mem} = \varepsilon_{mem} + \frac{\sigma_{mem}}{j\omega}, \quad (10)$$

$$\tilde{\varepsilon}_{int} = \varepsilon_{int} + \frac{\sigma_{int}}{j\omega}, \quad (11)$$

Here, d_{mem} denotes the membrane thickness and r_{cell} is the cell radius, with the thin shell assumption $d_{mem} \ll r_{cell}$. The numerator of equation (9) can be recast in terms of the specific membrane capacitance C_{mem} and conductance G_{mem}:

$$\frac{\tilde{\varepsilon}_{mem}}{d_{mem}} = \frac{\varepsilon_{mem}}{d_{mem}} + \frac{\sigma_{mem}}{j\omega d_{mem}} = C_{mem} + \frac{G_{mem}}{j\omega}. \quad (12)$$

TWO-SHELL YEAST MODEL

According to the two-shell model, the effective complex permittivity of the cell, $\tilde{\varepsilon}_{cell}$, is given by (Cottet et al., 2019):

$$\tilde{\varepsilon}_{cell} = \tilde{\varepsilon}_{wall}\frac{1 + 2\Psi\bar{F}_{CM}}{1 - \Psi\bar{F}_{CM}}, \quad (13)$$

where $\tilde{\varepsilon}_{wall}$ is the complex permittivity of the wall:

$$\tilde{\varepsilon}_{wall} = \varepsilon_{wall} + \frac{\sigma_{wall}}{j\omega}, \quad (14)$$

Ψ is the ratio between the volume of the intracellular compartment and the total cell volume, i.e.:

$$\Psi = (r^{int}/r^{cell})^3 \quad (15)$$

and

$$\bar{F}_{CM} = \frac{\tilde{\varepsilon}_{int\&mem} - \tilde{\varepsilon}_{wall}}{\tilde{\varepsilon}_{int\&mem} + 2\tilde{\varepsilon}_{wall}}, \quad (16)$$

with $\tilde{\varepsilon}_{int\&mem}$ given by the right-hand side of eq. (8). In this formulation, $\tilde{\varepsilon}_{int\&mem}$ represents the equivalent homogenized complex permittivity of the union of the intracellular compartment and the (thin) plasma membrane. Equations (13) and (16) then describe the further homogenization of this inner equivalent medium with the (thick) cell wall, yielding the overall effective complex permittivity $\tilde{\varepsilon}_{cell}$.

Table S1. Collection of model parameters. Fitted parameters are highlighted in light orange. (ε_0, vacuum permittivity)

	Initial value (for fitted parameters) or assumed value (for non-fitted parameter)	References/Notes
RBC – single-shell model		
r_{cell} [µm]	3.5	
$\sigma_{int} = \sigma_{cyt}$ [S/m]	0.6	
ε_{int} [F/m]	$65\varepsilon_0$	(Spencer and Morgan, 2020)
C_{mem} [µF/cm^2]	0.84	
G_{mem} [S/m^2]	0	(Spencer and Morgan, 2020)
σ_{med} [S/m]	0.996	Measured
ε_{med} [F/m]	$80\varepsilon_0$	(Spencer and Morgan, 2020)
Yeast – two-shell model		
r_{cell} [µm]	3.5	
r_{int} [µm]	$\sqrt[3]{0.8}\,r_{cell}$	i.e., the intracellular volume is 80% of the whole volume, in agreement e.g. with (Patel et al., 2012)
σ_{int} [S/m]	0.6	
ε_{int} [F/m]	$58\varepsilon_0$	(Haandbæk et al., 2016)
C_{mem} [µF/cm^2]	0.70	
G_{mem} [S/m^2]	0	(Haandbæk et al., 2016)
σ_{wall} [S/m]	$0.1\sigma_{med}$	(Asami et al., 1996)
ε_{wall} [F/m]	$60\varepsilon_0$	(Haandbæk et al., 2016)
σ_{med} [S/m]	0.733	Measured
ε_{med} [F/m]	$80\varepsilon_0$	(Haandbæk et al., 2016)
Polystyrene beads		
r_{bead} [µm]	2.25	Measured (by the manufacturer)
σ_{bead} [S/m]	0.9×10^{-3}	(Haandbæk et al., 2016)
ε_{bead} [F/m]	$2.5\varepsilon_0$	(Spencer and Morgan, 2020)

S5. SINGLE-SHELL MODEL SENSITIVITY ANALYSIS

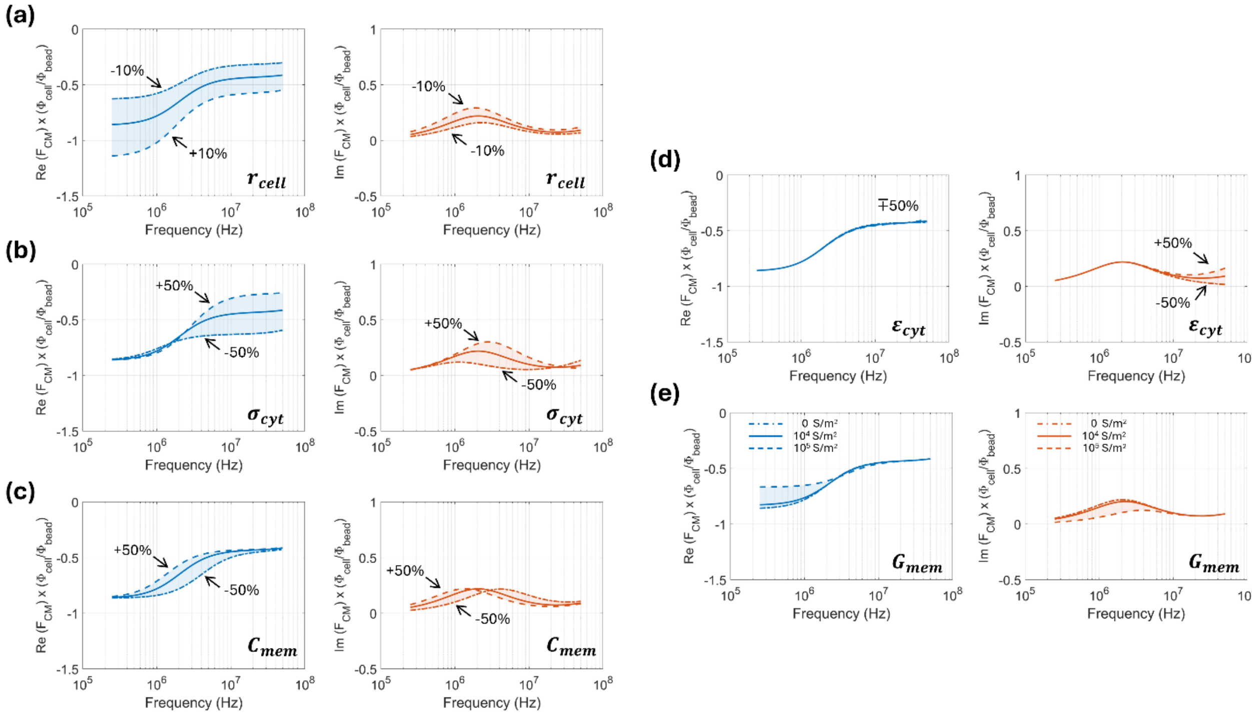

Fig. S5. Calculated examples of the real and imaginary parts of the cell Clausius-Mossotti factor multiplied by Φ^{cell}/Φ^{bead}, using the single-shell model. The continuous lines pertain to a reference cell with properties set as those of the median spectrum of the control RBC population (i.e., $r = 2.7$ µm, $C_{mem} = 0.97$ µF/cm^2, $\sigma_{cyt} = 0.41$ S/m; other parameters are as per Table S1). The dotted and dash-dotted lines pertain to a cell with modified parameters − one parameter at a time − as indicated within the respective plots. It can be noticed that, while cell radius, membrane capacitance, and cytoplasm conductivity have an appreciable effect on the spectrum over the tested frequency range, variations in cytoplasm permittivity become relevant only in the imaginary part at high frequencies. Furthermore, membrane conductance, which is usually considered as negligible, must reach very high values (~10^5 S/m^2) to have an appreciable effect on the impedance spectrum.

S6. METHYLENE BLUE ASSAY

Yeast heat-induced damage was assessed following a standard protocol. Equal volumes of yeast suspension (yeasts in PBS) and 0.1% (w/v) Methylene Blue were mixed, and after two minutes a 10 μL aliquot was examined in a counting chamber (FAST READ 102®, Biosigma). For the control sample, 368 cells were counted: 317 (86%) remained unstained, while 51 (14%) took up the dye and appeared dark. For the heat-treated sample, 282 cells were counted: 5 (2%) remained unstained, whereas 277 (98%) took up the dye and appeared dark. Representative images are shown in Fig. S6.

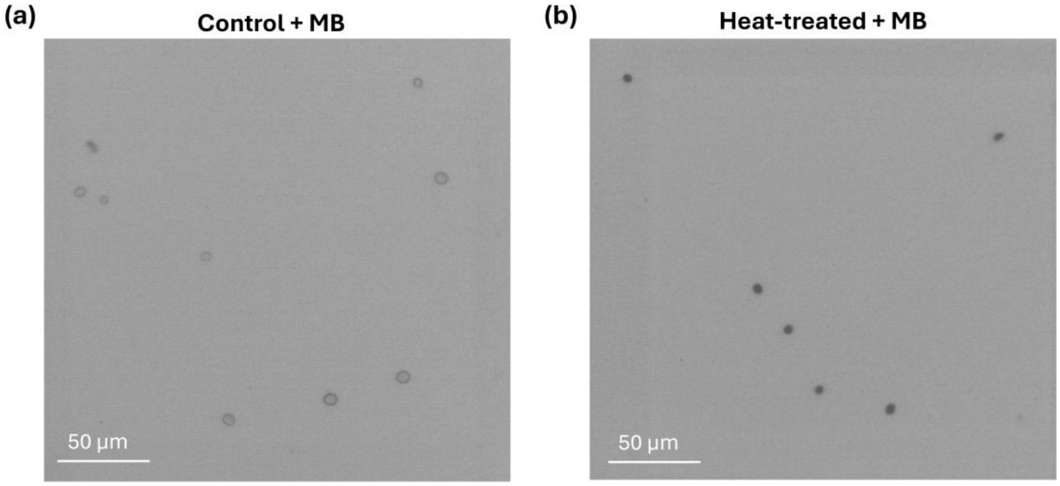

Fig. S6. Representative microscopy images of yeasts suspended in PBS + Methylene Blue (MB): (a) control sample, (b) heat-treated sample. Each image refers to one sector of the FAST READ 102® chamber.

S7. PRELIMINARY EXPERIMENTAL SESSIONS

When developing our methodology, we performed preliminary experimental sessions aimed at demonstrating that the reconstructed impedance spectra are not biased by zone-specific transfer functions.

The HF2IS and the HF2LI have 8 and 6 demodulators, respectively. In the preliminary sessions, we considered a total of 12 frequencies, so that the same number of frequency channels (i.e., 6) could be used in each device. Specifically, we considered: 0.50, 0.76, 1.16, 1.76, 2.67, 4.06, 6.16, 9.37, 14.24, 21.64, 32.90, and 50.00 MHz, and the subsets:

- LF (low frequencies): 0.50, 0.76, 1.16, 1.76, 2.67, 4.06 MHz,
- HF (high frequencies): 6.16, 9.37, 14.24, 21.64, 32.90, 50.00 MHz,
- OD (odd frequencies): 0.50, 1.16, 2.67, 6.16, 14.24, 32.90 MHz,
- EV (even frequencies): 0.76, 1.76, 4.06, 9.37, 21.64, 50.00 MHz.

We performed several measurements where we varied:

- the frequency set of each device (i.e., LF to HF2IS and HF to HF2LI, and vice versa; OD to HF2IS and EV to HF2LI, and vice versa),
- the measurement zone of each device (HF2IS connected to measurement zone A and HF2LI connected to measurement zone B, and vice versa),
- the gain of the transimpedance amplifier of each device (i.e., 1 kΩ and 10 kΩ).

The analysis showed that:

- the two devices, HF2IS and HF2LI, are equivalent.
- the two measurement zones, A and B, are generally equivalent. In one test, the low frequency signals had suboptimal quality when measured from one of the two measurement zones, probably due to partial electrode deterioration. Using the OD/EV partition instead of the LF/HF partition mitigated this issue.
- it is preferable to use 1 kΩ gain rather than 10 kΩ gain, which decreased the SNR of low-frequency channels.

As an example, Fig. S7 shows that the HF2IS and the HF2LI provide the same characterization of 4.5 µm beads across all tones. Moreover, it can be noticed that while the bead signal remains substantially stable up to 9 MHz, at higher frequencies it exhibits a frequency-dependent variation, which may be due to the electronic circuitry of the two devices. Calibration with co-flowing beads is therefore important to properly reconstruct cell impedance spectra.

Overall, in developing our methodology we performed several experimental sessions (across a six-month period), and we used a few different chips. The analysis of the measured signals showed good reproducibility between runs.

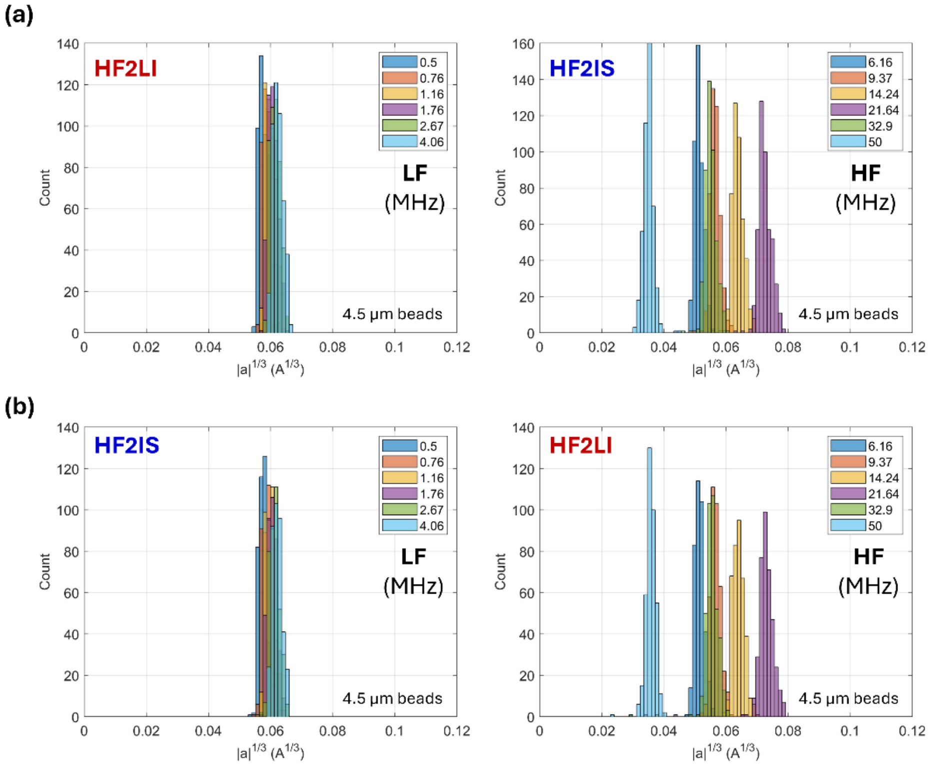

Fig. S7. Histogram of cube root of measured signal amplitude ($|a|^{1/3}$) for 4.5 µm beads, under two different configurations: (a) low frequencies (LF) assigned to HF2LI and high frequencies (HF) assigned to HF2IS, and vice versa in (b).

S8. ANALYSIS OF CELL MOTION THROUGH THE SENSING REGION

In our experimental setup, the channel cross section is 40 μm × 10 μm. Accordingly, a flow rate of 4 μL/min gives an average velocity of 0.167 m/s. The length of each measurement zone is L_{mz} =56 μm, while the distance between the centres of the two measurement zones is $L = 160$ μm. Therefore, the average measurement time in each zone and the average time separation between the two zones are 0.34 ms and 0.96 ms, respectively.

Those nominal figures were confirmed experimentally. Fig. S8(a) and (b) show a comparison of particle velocity distributions computed using either measurement zone A or measurement zone B (for a typical experiment). Median values and interquartile ranges are: 0.163 [0.155-0.176] m/s for measurement zone A, and 0.165 [0.156-0.176] m/s for measurement zone B. The analysis suggests that particle velocity remains rather stable across the two measurement zones.

Particle velocity is used to estimate the delay $\Delta = L/v$ between the two measurement zones, which in turn is used to set the initial condition for the event central time in the feature-extraction routine. Considering a velocity $v = 0.165$ m/s, a 10% error in velocity estimation results in an error E on Δ of about $E = 0.10\ L\ /v = 0.097$ ms. With a sampling rate of 28.8 kHz, this amounts to 2.8 samples. For slower particles ($v =$ 0.1 m/s) an error of 4.6 samples is obtained. The feature extraction routine, based on a multi-frequency bipolar Gaussian template, is robust with respect to non-optimal initial conditions and can handle inaccuracies of a few samples.

The transit times through each zone are: 0.344 [0.318–0.361] ms for measurement zone A, and 0.340 [0.319–0.359] ms for measurement zone B. Each event is therefore described by 9–10 samples. The histogram of the centre-to-centre time is shown in Fig. S8(c). Median values and interquartile ranges are: 0.984 [0.908-1.031] ms. The analysis of synchronized videos showed no evident variation of particle trajectory, orientation, or shape across the two measurement zones in the image plane (Fig. S9). Different particles may exhibit different trajectory and, for RBCs, also different orientation/shape, which introduces a blurring in the estimated dielectric properties. In the present coplanar electrode layout, the largest effect is associated to particle trajectory height (Errico et al., 2017). Orientation effects could be removed by using sphered RBCs (Spencer and Morgan, 2020).

No indications of measurement-induced cell perturbations were observed. In our continuous flow configuration, heat and electrochemical reaction products are continuously removed from the sensing region. Moreover, faradaic/electrochemical effects are reduced at frequencies above 250 kHz. The symmetric shape of the signal traces indicates that dielectric properties remain essentially unchanged within each measurement zone. Likewise, comparing the traces from the two zones shows no appreciable alteration in dielectric properties during transit through the sensing region. This observation is consistent with the fact that the dielectric properties we estimate for native RBCs align well with values reported in the literature for healthy cells (Salahi et al., 2022; Spencer and Morgan, 2020).

As discussed in our previous work (Caselli et al., 2020), the expected fraction of coincidences can be estimated by the product of the concentration and the measurement zone volume. In our setup, the measurement zone volume is 56 μm (length) × 40 μm (width) × 10 μm (height). With a concentration of 10^6 particles/mL, the fraction of coincidences is therefore small (about 2%). We found examples of coincidences in the electrical recordings, which have a 5-minute duration, but we did not catch any coincidences during the synchronized video acquisition, which lasted only 18 seconds.

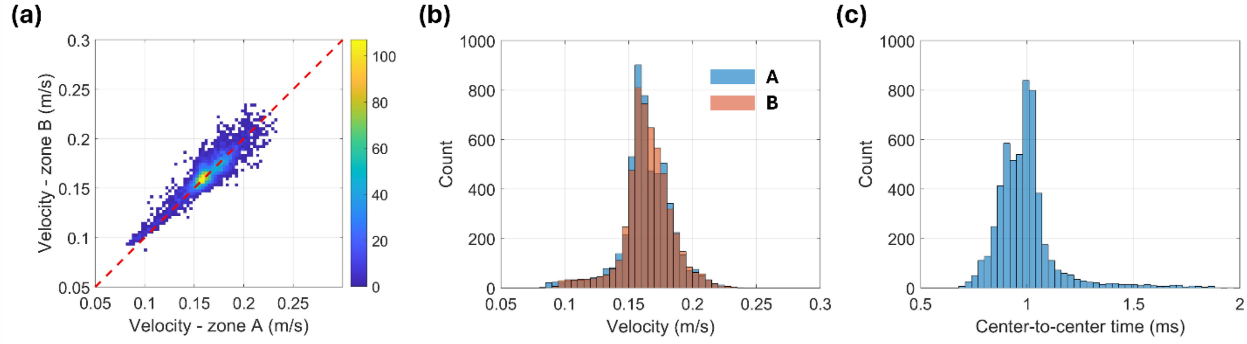

Fig. S8. (a) Density plot and (b) histogram of particle velocity obtained from impedance traces in measurement zone A versus measurement zone B. (c) Distribution of particle transit times from the centre of measurement zone A to the centre of measurement zone B (based on the impedance traces from measurement zone A). Reported data are relevant to an experiment with untreated RBCs and co-flowing beads.

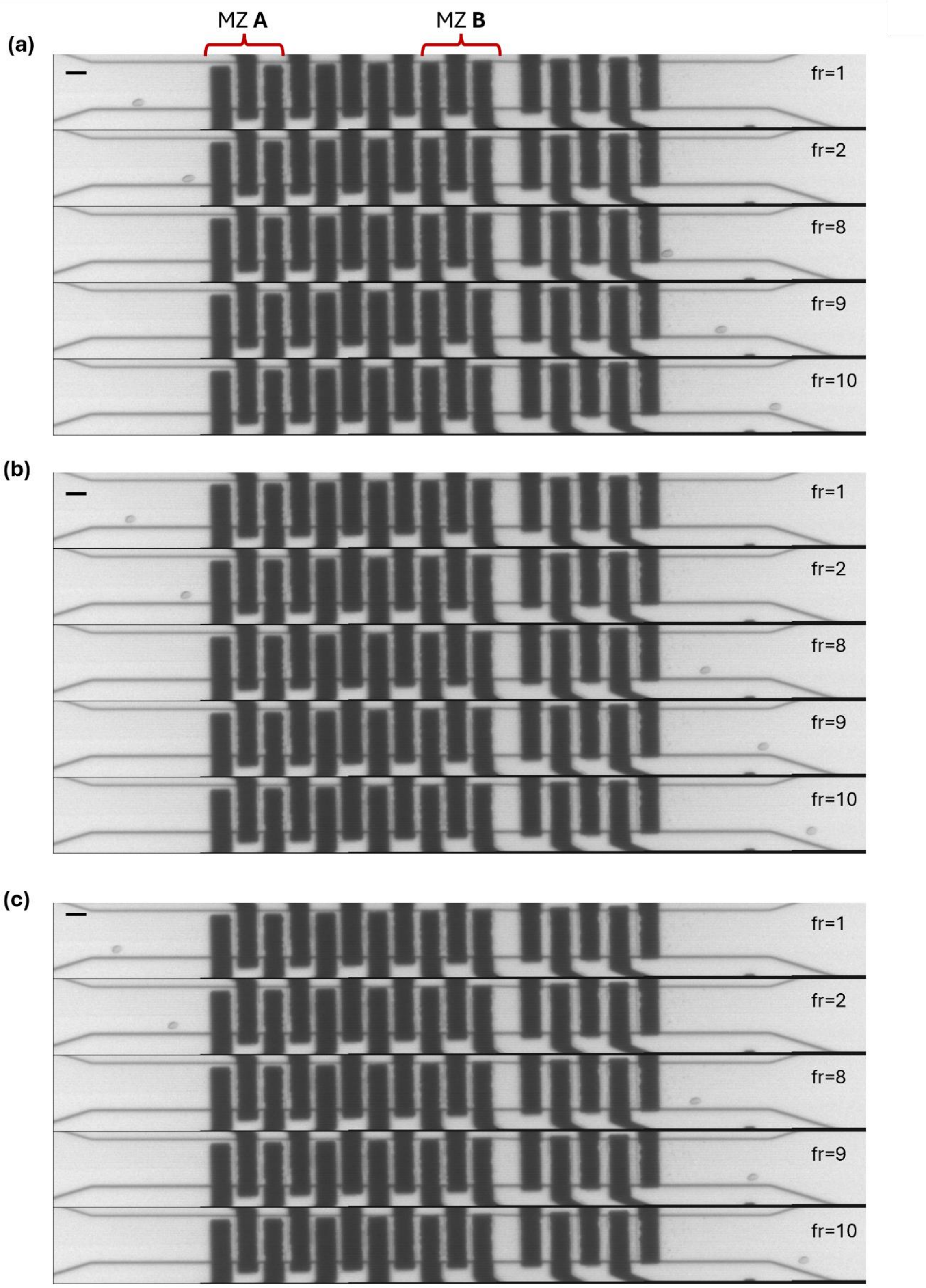

Fig. S9. Representative examples of RBCs traveling through the sensing region. For each cell, five frames (fr) are shown. Frames 1 and 2 show the cell approaching measurement zone A (MZ A), frames 8−10 show the cell past the electrode region. The five electrodes following measurement zone B (MZ B) are unused (i.e., floating). Scale bar is 15 µm.

S9. SUPPLEMENTARY DATA RELATED TO RBC ELECTRICAL CHARACTERIZATION

The presence of two distinct RBC subpopulations after AMP exposure, one retaining native-like dielectric properties and another showing altered characteristics, likely reflects the heterogeneous nature of peptide-membrane interactions. Several factors may contribute. First, different cells may exhibit heterogeneous peptide uptake, due e.g. to local microenvironment, or cell surface differences. Furthermore, cells receiving similar peptide exposure may exhibit different susceptibility because of intrinsic state differences (age, ATP level, membrane composition, cytoskeletal integrity, channel expression), that could affect peptide binding and insertion efficiency. Consequently, some cells may accumulate sufficient peptide to reach a threshold necessary to perturb the membrane, while others remain below the threshold without any significant dielectric changes. The RBC subpopulation with altered dielectric properties may represent cells where membrane perturbation has occurred inducing partial leakage/permeabilization without complete membrane disruption.

While at 1 μM DNS-PMAP23 only an RBC subpopulation with altered properties is found (Fig. 2(c) of the main text), in our previous study (Troiano et al., 2023), at concentrations < 1 μM we also observed an RBC subpopulation with native-like properties. The relative fraction of the two subpopulations correlated with the peptide concentration (cf. details in Fig. S10).

On the other hand, while two RBC subpopulations (altered or native-like) are observed for 20 μM trichogin GA IV (Fig. 2(e) of the main text), only the one with properties similar to those of native RBCs is found at 1 μM (Fig. S11).

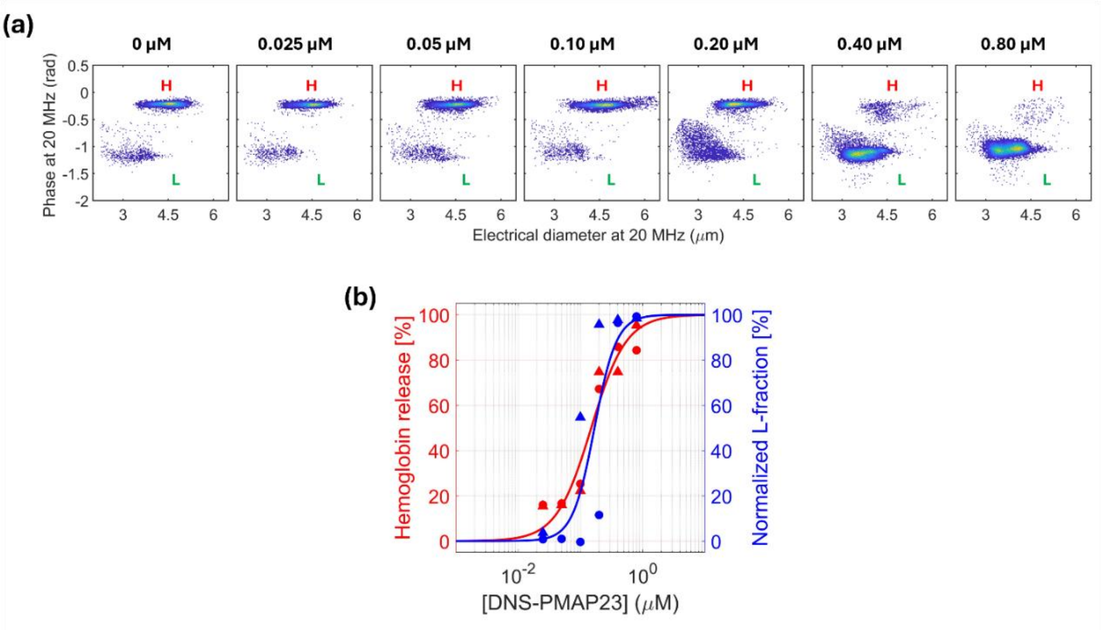

Fig. S10. Dose-response curve for RBCs incubated with DNS-PMAP23. Adapted from our previous work (Troiano et al., 2023), © 2023 The Authors. (a) Electrical phase (20 MHz) versus electrical diameter (20 MHz) for different peptide concentrations in the range 0−0.80 μM. Two RBC subpopulations are observed: the subpopulation with a higher phase is denoted by H and the one with lower phase is indicated by L. The relative fraction of the two subpopulations varies across the samples. In the negative control sample (0 μM) and at low peptide concentration (up to 0.10 μM in this representative example), subpopulation H is markedly dominant. At 0.20 μM, both subpopulations are well represented, whereas at 0.40 and 0.80 μM, subpopulation L is markedly dominant. Whereas cells belonging to subpopulation H were clearly identifiable in synchronized high-speed videos, cells belonging to subpopulation L turned out to be invisible. (b) Comparison of the RBC toxicity assay based on microfluidic impedance cytometry (at 20 MHz), in blue, with the standard toxicity assay based on haemoglobin release, in red. Markers denote experimental data points (circles and triangles refer to RBCs from two different donors), and continuous lines denote fits of the results using the Hill model.

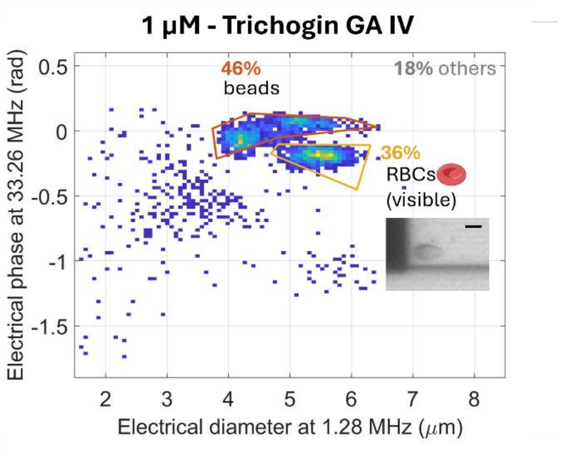

Fig. S11. Electrical phase (33.26 MHz) versus electrical diameter (1.28 MHz) at 1 μM trichogin GA IV. At this trichogin concentration, only the RBC subpopulation with electrical (and optical) features like those of the native cells is found. The scale bar in the inset is 5 μm.

S10. SUPPLEMENTARY INFORMATION ON RBC SPECTRA FITTING

Table S2 compares RBC fit results obtained either by fixing G_{mem} to 0 S/m^2 (as in Table 1 of the main text) or by treating G_{mem}, as a free fitting parameter. It can be noticed that the fitted values for r, C_{mem}, and σ_{cyt} are rather stable. On the other hand, a large uncertainty is associated to the fitted value for G_{mem}. Accordingly, we prefer to keep G_{mem} fixed to 0 S/m^2 elsewhere in this work. The distributions of fit error are reported in Fig. S12.

A nonparametric statistical analysis of the fitted dielectric parameters was performed. The Kruskal–Wallis test revealed significant group differences for r, C_{mem}, and σ_{cyt} ($p < 0.001$) across the three RBC groups (control, DNS-PMAP23, trichogin GA IV). Subsequent pairwise Mann–Whitney U tests indicated that both DNS-PMAP23 and trichogin GA-IV differed significantly from the control for all parameters after Bonferroni correction ($p < 0.001$). Pairwise correlations among parameters were weak to moderate (Table S3), and Cliff's delta values indicated strong effect sizes (Table S4).

Table S2. Comparison of RBC fit results obtained with G_{mem} fixed or free. For each experimental condition, the median values and interquartile ranges of the single-cell fits are reported (N, number of single-cell spectra).

Sample	N	Radius $\boldsymbol{r}$ (µm)	Membrane capacitance $\boldsymbol{C_{mem}}$ (µF/cm^2)	Cytoplasm conductivity $\boldsymbol{\sigma_{cyt}}$ (S/m)	Membrane conductance $\boldsymbol{G_{mem}}$ (S/m^2)
Control	3864	2.7 [2.6-2.8]	0.95 [0.81-1.1]	0.41 [0.39-0.44]	0 (fixed)
Control – $\boldsymbol{G_{mem}}$ free	3864	2.7 [2.6-2.9]	1.1 [0.88-1.3]	0.43 [0.41-0.47]	4 [0.72-8300]
DNS-PMAP23 (1 µM)	10399	3.1 [2.9-3.2]	0.48 [0.44-0.53]	0.96 [0.94-0.98]	0 (fixed)
DNS-PMAP23 (1 µM) – $\boldsymbol{G_{mem}}$ free	10399	3.1 [2.9-3.2]	0.48 [0.45-0.53]	0.96 [0.95-0.98]	20 [1.8-140]
Trichogin GA IV (20 µM)	6903	1.9 [1.8-2.1]	0.56 [0.48-0.63]	0.82 [0.74-0.89]	0 (fixed)
Trichogin GA IV (20 µM) – $\boldsymbol{G_{mem}}$ free	6903	2 [1.8-2.2]	0.58 [0.49-0.68]	0.86 [0.78-0.93]	14 [1.1-1900]

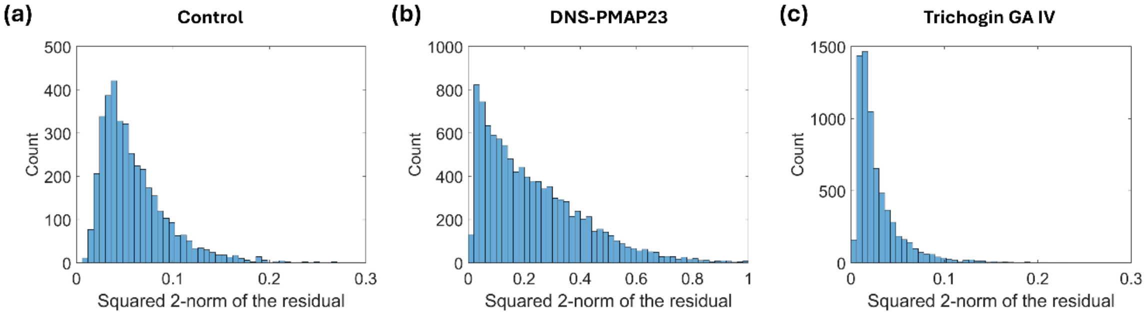

Fig. S12. Distribution of the squared 2-norm of the residual pertinent to the fit of individual RBC spectra, for the three experimental conditions: (a) control, (b) 1 µM DNS-PMAP23, and (c) 20 µM trichogin GA IV.

Table S3. Pairwise correlations between the fitted dielectric parameters, for each experimental condition.

Sample	N	Correlation $\boldsymbol{r}$ - $\boldsymbol{C_{mem}}$	Correlation $\boldsymbol{r}$ - $\boldsymbol{\sigma_{cyt}}$	Correlation $\boldsymbol{C_{mem}}$ - $\boldsymbol{\sigma_{cyt}}$
Control	3864	-0.085	0.186	0.324
DNS-PMAP23 (1 µM)	10399	-0.126	0.178	-0.274
Trichogin GA IV (20 µM)	6903	-0.240	0.421	-0.455

Table S4. Cliff's Delta and related confidence interval (CI), for each fitted dielectric parameter, in pairwise comparisons of the control sample versus the treated samples.

Pairwise comparison	Cliff's Delta (value and CI)		
	r (µm)	C_{mem} (µF/cm^2)	σ_{cyt} (S/m)
Control vs DNS-PMAP23 (1 µM)	-0.910 [-0.915, -0.902]	0.985 [0.981, 0.988]	-1 [-1, -1]
Control vs Trichogin GA IV (20 µM)	0.998 [0.998, 0.999]	0.868 [0.857, 0.878]	-0.954 [-0.960, -0.947]

S11. MANUAL IMAGE-BASED GATING OF HEAT-TREATED YEASTS

For each electrical event, three consecutive image frames were shown to the annotator (Fig. S13). In the resulting montage it was easy to identify the traveling particle. The annotator was asked to click on one of the three letters shown below the montage: O, for other (e.g., debris); B, for bead; Y, for yeast. To gain familiarity with the appearance of beads and yeasts, the annotator was initially trained with images taken from single-population experiments. Beads are characterized by a circular shape of consistent size and good contrast. Conversely, yeasts are less regular, more heterogeneous in size, and exhibit lower contrast. Overall, distinguishing beads from yeast cells is feasible. Consensus among two independent annotators was used. As a future perspective, to avoid the need of manual labelling, beads of a different size could be used, whose electrical diameter does not overlap with that of the yeasts.

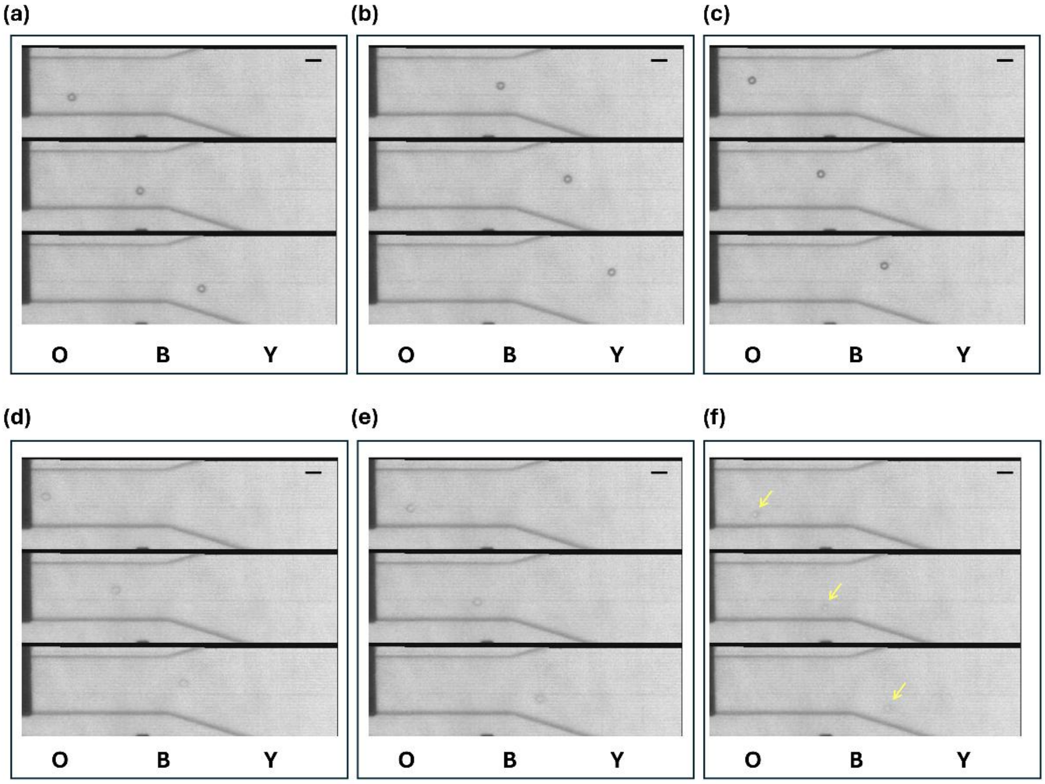

Fig. S13. Examples of three-frame montages shown to the annotator for classification (O, other; B, bead; Y, yeast). (a)-(c) Examples of flowing beads. (d)-(f) Examples of flowing yeasts. In panel (f), an arrow indicates the cell for the reader's convenience. Scale bar is 10 µm. The data are relevant to the experiment in Figure 4(c) of the main text.

S12. GALLERY OF IMPEDANCE SPECTRA OF SINGLE YEAST CELLS

Representative examples of single-cell spectra of yeast cells are shown in Fig. S14.

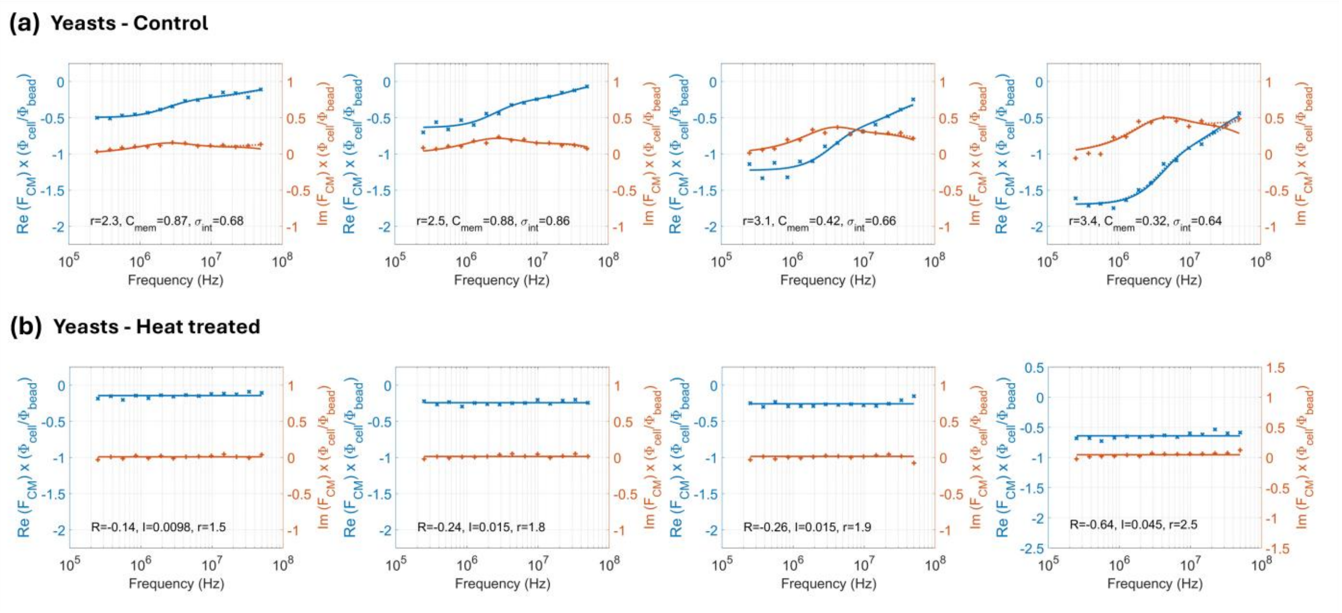

Fig. S14. Fourteen-frequency impedance spectra of single yeast cells. Four examples for each experimental condition are shown: (a) control, (b) heat-treated sample. Data points denote the experimental measurements, while solid lines denote (a) their fit using the two-shell model and (b) a constant fit. For each example in (a), the fitted model parameters are also indicated (r, radius in μm; C_{mem}, membrane capacitance in μF/cm^2; σ_{int}, cytoplasm conductivity in S/m). Moreover, a fit obtained by setting ε_{int} free is also shown (dotted lines). For each example in (b), the real and imaginary parts of the constant fit (denoted by R and I, respectively) and the values of the radius r estimated assuming a Clausius-Mossotti factor $F_{CM} = -0.45$ are also indicated.

S13. PARTICLE THROUGHPUT OVER TIME

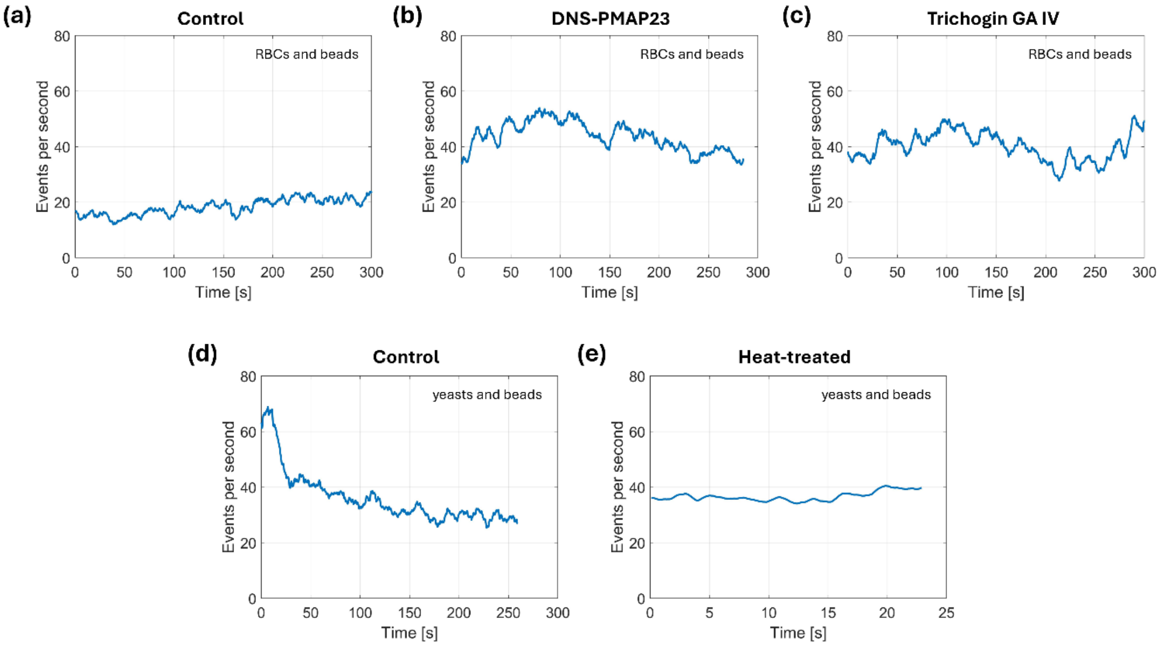

Fig. S15. Time behaviour of particle throughput (i.e., number of acquired events per second, averaged over a 10-second window). (a-c) RBC tests: control, 1 µM DNS-PMAP23, and 20 µM trichogin GA IV. (d-e) Yeast tests: control and heat-treated sample. For all the experimental conditions (except (e)) acquisitions of about 5 minutes were performed. A shorter acquisition was conducted for the heat-treated sample (e) due to the hardware limitations of the high-speed system used for simultaneous image acquisition. The typical overall throughput (i.e., cells and beads) is on the order of 40 events per second. This value is slightly lower than expected from the nominal concentration and flow rate, possibly due to an overestimation of the initial sample concentration or to sedimentation within the syringe. In a local time window, a maximum cell throughput of 40 cells per second is reached (i.e., RBCs in panel (b), during the second minute of the acquisition).

S14. SURVEY OF SINGLE-CELL IMPEDANCE SPECTROSCOPY APPROACHES

Table S5. Impedance spectroscopy (IS) approaches for single-cell characterization. The selection of trapped-cell approaches is non-exhaustive, three representative examples are reported. Impedance cytometry approaches that characterize cell electrical features at a few frequencies but do not reconstruct the cell impedance spectrum are not included. Frequency resolution is computed as $N/log_{10}(f_2/f_1)$, where N is the number of frequency points, and f_1 and f_2 denote the lowest and highest frequency, respectively. N/A, not available; dp, data points.

Approach	**Reference**	**Frequency range and number of frequencies**	**Frequency resolution**	**Numerosity and throughput**	**Sample type and application**
IS of single **trapped** cells	(Wang et al., 2011)	11 kHz–101 kHz; 10-point sweep	10.4 dp/decade	A few cells; N/A	HeLa cells and MCF-7 cells; cell characterization
	(Zhu et al., 2014)	10 kHz–10 MHz; 92-point sweep	30.6 dp/decade	Tens of cells; N/A	Yeast cells (S. cerevisiae); cell-growth monitoring
	(El Hasni et al., 2017)	100 Hz–10 MHz; 300-point sweep	60 dp/decade	A few cells; N/A	Oocytes (with and without zona pellucida); studying the influence of zona pellucida
IS of single **flowing** cells	(Spencer and Morgan, 2020)	250 kHz–50 MHz; 8 simultaneous, logarithmically spaced	3.5 dp/decade	Thousands of cells; 200 spectra/s	Red blood cells (spherocytes and ghosts); cell characterization
	(Zou et al., 2025)	250 kHz–550 MHz; 8 simultaneous, logarithmically spaced	2.4 dp/decade	Thousands of cells; 250 spectra/s	HL60 cells (untreated and fixed) and THP-1 cells (before and after differentiation); cell characterization
	Present work	250 kHz–50 MHz 14 simultaneous, logarithmically spaced	6.1 dp/decade	Thousands of cells; 40 spectra/s	Red blood cells (untreated and exposed to AMPs) and yeast cells (untreated and heat-treated); cell characterization

References

Asami, K., Yonezawa, T., Wakamatsu, H., Koyanagi, N., 1996. Dielectric spectroscopy of biological cells. Bioelectrochem. Bioenerget. 40, 141–145. https://doi.org/10.1016/0302-4598(96)05067-2

Caselli, F., De Ninno, A., Reale, R., Businaro, L., Bisegna, P., 2020. A Bayesian Approach for Coincidence Resolution in Microfluidic Impedance Cytometry. IEEE Trans Biomed Eng 68, 340–349. https://doi.org/10.1109/TBME.2020.2995364

Cottet, J., Fabregue, O., Berger, C., Buret, F., Renaud, P., Frénéa-Robin, M., 2019. MyDEP: A New Computational Tool for Dielectric Modeling of Particles and Cells. Biophys. J. 116, 12–18. https://doi.org/10.1016/j.bpj.2018.11.021

El Hasni, A., Schmitz, C., Bui-Göbbels, K., Bräunig, P., Jahnen-Dechent, W., Schnakenberg, U., 2017. Electrical impedance spectroscopy of single cells in hydrodynamic traps. Sens. Actuators B Chem. 248. https://doi.org/10.1016/j.snb.2017.04.019

Errico, V., De Ninno, A., Bertani, F.R., Businaro, L., Bisegna, P., Caselli, F., 2017. Mitigating positional dependence in coplanar electrode Coulter-type microfluidic devices. Sens. Actuators B Chem. 247, 580–586. https://doi.org/10.1016/j.snb.2017.03.035

Haandbæk, N., Bürgel, S.C., Rudolf, F., Heer, F., Hierlemann, A., 2016. Characterization of Single Yeast Cell Phenotypes Using Microfluidic Impedance Cytometry and Optical Imaging. ACS Sens 1, 1020–1027. https://doi.org/10.1021/acssensors.6b00286

Honrado, C., Bisegna, P., Swami, N.S., Caselli, F., 2021. Single-cell microfluidic impedance cytometry: from raw signals to cell phenotypes using data analytics. Lab Chip 21, 22–54. https://doi.org/10.1039/D0LC00840K

Patel, S., Showers, D., Vedantam, P., Tzeng, T.R., Qian, S., Xuan, X., 2012. Microfluidic separation of live and dead yeast cells using reservoir-based dielectrophoresis. Biomicrofluidics 6. https://doi.org/10.1063/1.4732800

Salahi, A., Honrado, C., Rane, A., Caselli, F., Swami, N.S., 2022. Modified Red Blood Cells as Multimodal Standards for Benchmarking Single-Cell Cytometry and Separation Based on Electrical Physiology. Anal. Chem. 94, 2865–2872. https://doi.org/10.1021/acs.analchem.1c04739

Spencer, D., Morgan, H., 2020. High-Speed Single-Cell Dielectric Spectroscopy. ACS Sens. 5, 423–430. https://doi.org/10.1021/acssensors.9b02119

Troiano, C., De Ninno, A., Casciaro, B., Riccitelli, F., Park, Y., Businaro, L., Massoud, R., Mangoni, M.L., Bisegna, P., Stella, L., Caselli, F., 2023. Rapid Assessment of Susceptibility of Bacteria and Erythrocytes to Antimicrobial Peptides by Single-Cell Impedance Cytometry. ACS Sens. 8, 2572–2582. https://doi.org/10.1021/acssensors.3c00256

Wang, M.H., Kao, M.F., Jang, L.S., 2011. Single HeLa and MCF-7 cell measurement using minimized impedance spectroscopy and microfluidic device. Review of Scientific Instruments 82. https://doi.org/10.1063/1.3594550

Zhu, Z., Frey, O., Franke, F., Haandbæk, N., Hierlemann, A., 2014. Real-time monitoring of immobilized single yeast cells through multifrequency electrical impedance spectroscopy. Anal. Bioanal. Chem. 406, 7015–7025. https://doi.org/10.1007/s00216-014-7955-9

Zou, X., Spencer, D.C., Morgan, H., 2025. Single-cell impedance spectroscopy of nucleated cells. Lab Chip 25, 2939–2948. https://doi.org/10.1039/D5LC00111K